



### 저작자표시-비영리-변경금지 2.0 대한민국

이용자는 아래의 조건을 따르는 경우에 한하여 자유롭게

- 이 저작물을 복제, 배포, 전송, 전시, 공연 및 방송할 수 있습니다.

다음과 같은 조건을 따라야 합니다:



저작자표시. 귀하는 원 저작자를 표시하여야 합니다.



비영리. 귀하는 이 저작물을 영리 목적으로 이용할 수 없습니다.



변경금지. 귀하는 이 저작물을 개작, 변형 또는 가공할 수 없습니다.

- 귀하는, 이 저작물의 재이용이나 배포의 경우, 이 저작물에 적용된 이용허락조건을 명확하게 나타내어야 합니다.
- 저작권자로부터 별도의 허가를 받으면 이러한 조건들은 적용되지 않습니다.

저작권법에 따른 이용자의 권리와 책임은 위의 내용에 의하여 영향을 받지 않습니다.

이것은 [이용허락규약\(Legal Code\)](#)을 이해하기 쉽게 요약한 것입니다.

[Disclaimer](#)



Master's Thesis of Science

# N-type doping of bilayer graphene devices by hydrogen adsorption

수소 흡착을 통한 이중층 그래핀 소자의 N-타입  
도핑

February 2016

Graduate School of Physics  
Seoul National University  
Physics Major

David Soler Delgado

# N-type doping of bilayer graphene devices by hydrogen adsorption

**Professor Yung Woo Park**

Submitting a master's thesis of Physics

December 2015

Graduate School of Physics  
Seoul National University  
Physics Major

David Soler Delgado

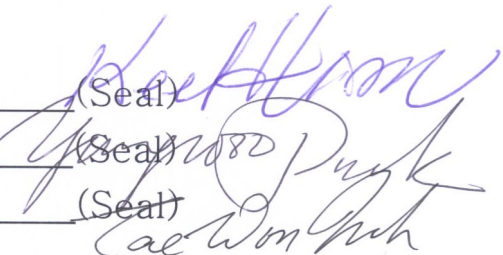
Confirming the master's thesis written by

David Soler Delgado

December 2015

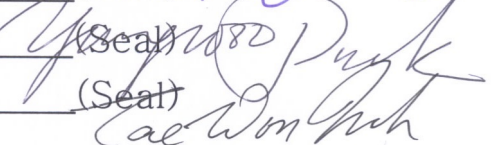
Chair Kee Hoon Kim

(Seal)



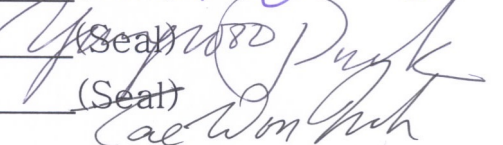
Vice Chair Yung Woo Park

(Seal)



Examiner Tae Won Noh

(Seal)



# **Abstract**

Hydrogenation of graphene has attracted attention due to the modified transport properties such as electron doping. Despite the fact that there has been studies of hydrogenation of exfoliated graphene, there are studies missing for bilayer graphene systems with higher degrees of complexity such as twisted bilayer graphene (tBLG).

In this thesis, we fabricated CVD-grown tBLG graphene devices and exposed them into high-pressure pure molecular hydrogen environment. By means of Raman spectroscopy and electrical characterization methods such as electrical transfer curve and Seebeck coefficient (TEP) measurements, the n-type doping behaviour is confirmed regardless of the twisting angle between the layers, suggesting the H<sub>2</sub> dissociation on the surface of graphene. Our results can be used as an aid for exploring further functionalities of hydrogenated bilayer graphene devices.

**Keyword:** twisted bilayer graphene, hydrogenation, electron doping, Seebeck coefficient.

**Student number:** 2013-23787

# Contents

<b>Abstract</b>	<b>i</b>
<b>1 Introduction</b>	<b>1</b>
1.1 Motivation . . . . .	1
1.1.1 The incursion of carbon in high-performance electronics . . . . .	1
1.1.2 Outline and purpose of this thesis . . . . .	4
<b>2 Background</b>	<b>8</b>
2.1 Single layer graphene . . . . .	8
2.2 Bilayer and twisted bilayer graphene . . . . .	10
2.3 Doping methods of graphene reviewed . . . . .	13
<b>3 Fabrication and experimental procedures</b>	<b>18</b>
3.1 Device Fabrication . . . . .	19
3.1.1 CVD-Growth of twisted bilayer graphene . . . . .	19
3.1.2 E-beam lithography . . . . .	21
3.1.3 Electrode deposition and graphene etching . . . . .	22

3.2	Characterization Techniques . . . . .	23
3.2.1	Raman Spectroscopy . . . . .	23
3.2.2	Electrical measurements . . . . .	25
3.3	Hydrogenation of Graphene devices . . . . .	29
<b>4</b>	<b>N-type doping on CVD-grown twisted bilayer graphene devices by hydrogen adsorption</b>	<b>34</b>
4.1	Identification of CVD-grown twisted bilayer graphene . .	34
4.2	Transfer curves of graphene devices under hydrogen exposure	38
4.3	Raman spectroscopy of hydrogenated tBLG . . . . .	40
4.4	TEP measurements of graphene device under hydrogen exposure . . . . .	42
4.5	Development of device features as hydrogen exposure . .	44
<b>5</b>	<b>Summary and Conclusion</b>	<b>49</b>

# List of Figures

1.1	Low dimensional allotropes of carbon. . . . .	2
1.2	Facts on graphene history. . . . .	3
2.1	Real and reciprocal lattices, and electronic dispersion relation for single layer graphene . . . . .	9
2.2	Real and reciprocal lattices, electronic dispersion and band gap opening for Bernal bilayer graphene . . . . .	10
2.3	Real and reciprocal lattices, electronic dispersion and van Hove singularities for twisted bilayer graphene . . . . .	12
2.4	Examples of graphene doping . . . . .	14
3.1	CVD-growth process and transfer . . . . .	19
3.2	3-step process fabrication of the graphene devices . . . .	21
3.3	Raman spectroscopy scattering processes and graphene spectrum . . . . .	23
3.4	Graphene field-effect transistor schematic and its transfer curve . . . . .	26

3.5	Thermo-electric power measurements schematic, principles and calibration . . . . .	28
3.6	Probe for cryostat and high H <sub>2</sub> pressure . . . . .	30
4.1	Measurement of twist angle of tBLG flakes . . . . .	35
4.2	Raman spectroscopy of tBLG devices with different stacking angles . . . . .	36
4.3	Transfer curves of all our devices as a function of time . .	39
4.4	Raman spectroscopy on the small angle sample before and after hydrogen exposure . . . . .	41
4.5	Seebach coefficient for the critical angle sample before and after hydrogen exposure . . . . .	43
4.6	V <sub>CNP</sub> for different twisted angle as a function of time . .	44
4.7	Evolution of carrier mobility as a H <sub>2</sub> time exposure . . .	45

# List of Tables

4.1	Fitted values of G and 2D peaks for small angle samples	37
4.2	Fitted values of G and 2D peaks, before and after hydrogen exposure . . . . .	40

# Chapter 1

## Introduction

### 1.1 Motivation

#### 1.1.1 The incursion of carbon in high-performance electronics

Since the early beginnings of high-performance electronics, the field effect transistor (FET) has been used as a main building block of our processing cores. As the time goes by, the Moore's law is pushing the limit on the dimensions of these devices up to the point that in some years, silicon, the commercially preferred material for micro/nano electronics, will be no longer usable [2]. In this approach, the nanotechnology and the condensed matter physics fields have a difficult task to find a suitable way of keep the computing power increasing as the device size does the opposite. Several ways have been attempted to overcome this issue, ranging from changing the processing paradigm by encoding information on different degrees of freedom of atoms and electrons, up to looking into novel transistor configuration, including the incorporation of new emergent materials.

Focusing on this last attempt, low-dimensional carbon allotropes have

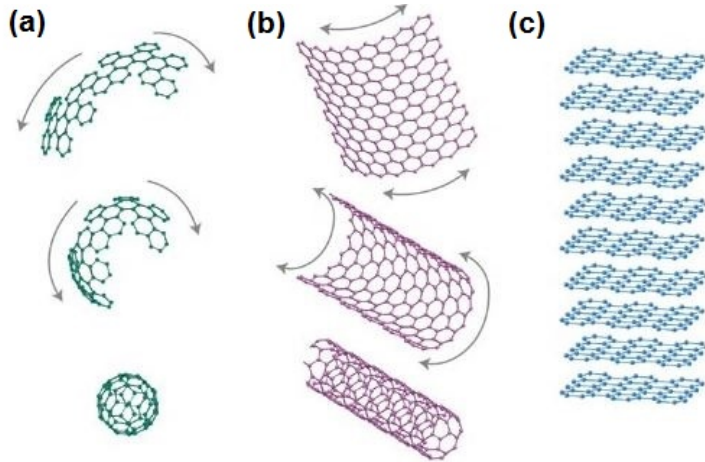


Figure 1.1: Low dimensional allotropes of carbon. (a) Fullerenes, caged configurations of carbon atoms grouped in a spherical shapes (b) Carbon nanotubes, (c) Stacks of single layer graphene. Adapted from [1]

been always considered as a strong candidate, reflected on the amount of research done on this field from its early beginnings. Starting from the zeroth dimensional material of the family, the fullerene [3] (Figure 1.1a), has been tried to be introduced in modern high-performance technologies as n-type channel on field effect transistors, by taking advantage of its solution processability [4]. However its performance is still inferior to the silicon-based well known technologies. Also, due to the interesting physics observed on the fullerene, there have been theoretical approaches exploring the spin degree of freedom of the molecule, in order to be used as a quantum-computer building block but unfortunately, its implementation seems far from now, quenching the chances of incursion of the fullerenes into the field of high-performance electronics in the near future. [5].

Following the discovery timeline, the one-dimensional material of the carbon family, the nanotubes (CNT's), was a bit more promising on its attempt to reach the commercial electronics field, due to their remarkable features such as an high carrier mobility of  $\sim 79,000 \text{ cm}^{-2}/\text{Vs}$  [6] and

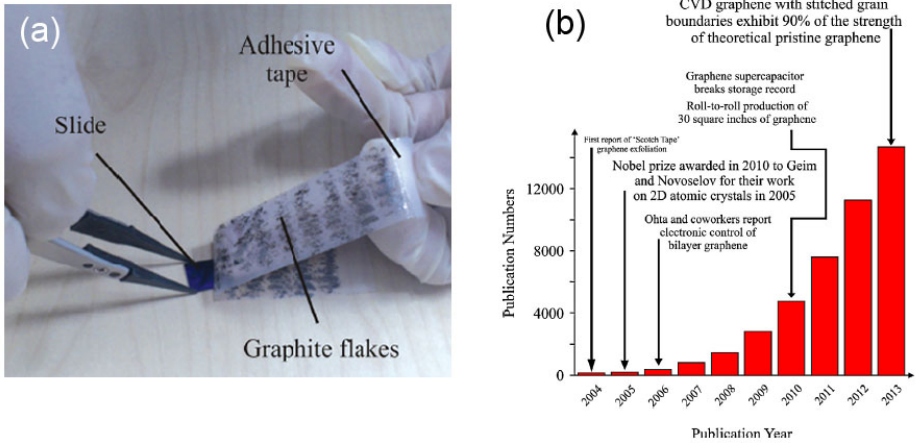


Figure 1.2: (a) Mechanical scotch tape method (b) Publication numbers of graphene after its discovery. Adapted from [8]

the important phenomena observed such as superconductivity and single ballistic transport [7]. Unfortunately, despite the fact of its superior properties of the CNT's, they has not reached the consumer high-performance electronics field either, tentatively suggested by the moderate difficulty on the device processing and manufacturing.

Lastly, graphene (Figure 1.1c), the two-dimensional member of the carbon family and the first two-dimensional material ever isolated, was discovered by Andre Geim and Kostya Novoselov in 2004. Its unique features such as the extremely high mobility ( $\sim 200,000 \text{ cm}^{-1}/\text{Vs}$ ) [9], the ease on device fabrication and the new emergent physics inside it, are not only making it one of the strongest silicon competitors, but also it is leading a revolution in the condensed matter research field as shown in the number of publications after graphene discovery (Figure 1.2b)[8].

However, despite the magnificent graphene characteristics, there are two crucial factors that might impede to reach this goal. The first of them is the production of large scale, high-quality graphene. Although it has

been possible to growth up to 30 inches of continuous sheet by chemical vapor deposition (CVD) methods [10], its carrier mobility is still inferior to the exfoliated graphene flakes obtained from highly oriented graphite (HOPG). The second issue is caused by the intrinsic nature of graphene which is a zero-gap semiconductor with the Fermi level located in the so called Dirac point. It is desirable for high-performance electronics to use gapped semiconductors with the chance of controlling the Fermi level, in order to create complementary electronic structures. Graphene has an extraordinary sensitivity to external environments, where simple interactions such as metal deposition [11], moisture [12] or even exposure to different type of gases and chemicals can induce doping and band-gap opening [13], [14]. Therefore, by finding suitable and robust treatments, it will be possible to tailor the graphene properties, making them fit into the requirements to substitute silicon on the high-performance electronics area.

### **1.1.2 Outline and purpose of this thesis**

In this thesis work, we contribute in finding some solution to the second of the problems previously addressed by studying the modification of bilayer graphene upon its exposure into 99.9999%  $H_2$  high-pressure environments. Despite the fact there has been some previous studies about this type of hydrogen interaction with exfoliated single and bilayer graphene [15], there is still a lack of research on the area of CVD-grown bilayer graphenes. Moreover, we exploit the advantages of the CVD method by growing hexagonal bilayer graphene flakes with a rotational mismatch between the layers, also know as twisted bilayer graphene (tBLG). Therefore, by adding this extra degree of complexity, it will be possible to extend our observations for those unexplored bilayer graphene systems, in order to give a broader options on the seek for a suitable graphene modification technique.

For this matter, the present manuscript is structured in the following manner: The following section, Chapter 2, will cover the background subjects whose enforce our motivation and give the necessary insights for the interpretation our data. In chapter 3, the methodology followed on the device fabrication, as well as experimental procedure will be described and justified in detail, whereas Chapter 4, considered as the central piece of this thesis, shows and discusses the major results that this work contributes to the graphene research field. Finally, Chapter 5 summarizes our experiments and findings, and addresses the possible pathways to follow for the future research.

# Bibliography

- [1] A. K. Geim and K. S. Novoselov, *Nature Materials*, 183–191 (2007).
- [2] D. Bishop, *Bell Labs Technical Journal* **10**, 23–28 (2005).
- [3] H. K. Kroto, J. R. Heath, S. C. O. Brien, R. L. Curl, and R. E. Smalley, *Nature* **318**, 162–163 (1985).
- [4] P. H. Wobkenberg, D. D. Bradley, D. Kronholm, J. C. Hummelen, D. M. de Leeuw, M. Cölle, and T. D. Anthopoulos, *Synthetic Metals* **158**, 468–472 (2008).
- [5] J. P. Connerade and V. K. Dolmatov, *Journal of Physics B: Atomic, Molecular and Optical Physics* **48**, 015007 (2015).
- [6] T. Durkop, S. A. Getty, E. Cobas, and M. S. Fuhrer, *Nano Letters* **4**, 35–39 (2004).
- [7] M. Terrones, *Annual Review of Materials Research* **33**, 419–501 (2003).
- [8] E. P. Randviir, D. A. Brownson, and C. E. Banks, *Materials Today* **17**, 426–432 (2014).
- [9] K. S. Novoselov, A. K. Geim, S. V. Morozov, D. Jiang, M. I. Katsnelson, I. V. Grigorieva, S. V. Dubonos, and A. A. Firsov, *Nature* **438**, 197–200 (2005).

- [10] S. Bae, H. Kim, Y. Lee, X. Xu, J.-S. Park, Y. Zheng, J. Balakrishnan, T. Lei, H. Ri Kim, Y. I. Song, Y.-J. Kim, K. S. Kim, B. Özyilmaz, J.-H. Ahn, B. H. Hong, and S. Iijima, *Nature Nanotechnology* **5**, 574–578 (2010).
- [11] Y. Nam, N. Lindvall, J. Sun, Y. W. Park, and A. Yurgens, *Carbon* **50**, 1987–1992 (2012).
- [12] H. Wang, Y. Wu, C. Cong, J. Shang, and T. Yu, *ACS Nano* **4**, 7221–7228 (2010).
- [13] Z. Chen, P. Darancet, L. Wang, A. C. Crowther, Y. Gao, C. R. Dean, T. Taniguchi, K. Watanabe, J. Hone, C. A. Marianetti, and L. E. Brus, *ACS Nano* **8**, 2943–2950 (2014).
- [14] A. J. Samuels and J. D. Carey, *ACS Nano* **7**, 2790–2799 (2013).
- [15] B. H. Kim, S. J. Hong, S. J. Baek, H. Y. Jeong, N. Park, M. Lee, S. W. Lee, M. Park, S. W. Chu, H. S. Shin, J. Lim, J. C. Lee, Y. Jun, and Y. W. Park, *Scientific Reports* **2** (2012).

# Chapter 2

## Background

### 2.1 Single layer graphene

Single layer graphene (SLG) is a one-atom thick, two-dimensional sheet of carbon atoms bonded to their in-plane neighbours due to the  $sp^2$  hybridized atomic orbitals, leading to the creation of one  $\pi$ -bond and three covalent  $\sigma$ -bonds and forming a triangular planar structure with an interatomic distance of 1.42 Å. This atomic structure give rise to the graphene honeycomb lattice that is best represented by a triangular bravais lattice with basis of two atoms per unit cell (A and B), as depicted on Figure 2.1a). The following primitive ( $a$ ) and basis vectors ( $\delta$ ) constitute the crystallographic description of graphene. [1]

$$a_1 = \frac{a}{2}(3, \sqrt{3}) \quad a_2 = \frac{a}{2}(3, -\sqrt{3}) \quad (2.1)$$

$$\delta_1 = (0, 0) \quad \delta_2 = -a(1, 0) \quad (2.2)$$

Thus, the hexagonal graphene structure facilitated the electronic band structure calculation by using the simplest approximation methods, such as the tight-binding method, with a high degree of accuracy on the low-energy region, where valence and conductance bands have a electronic

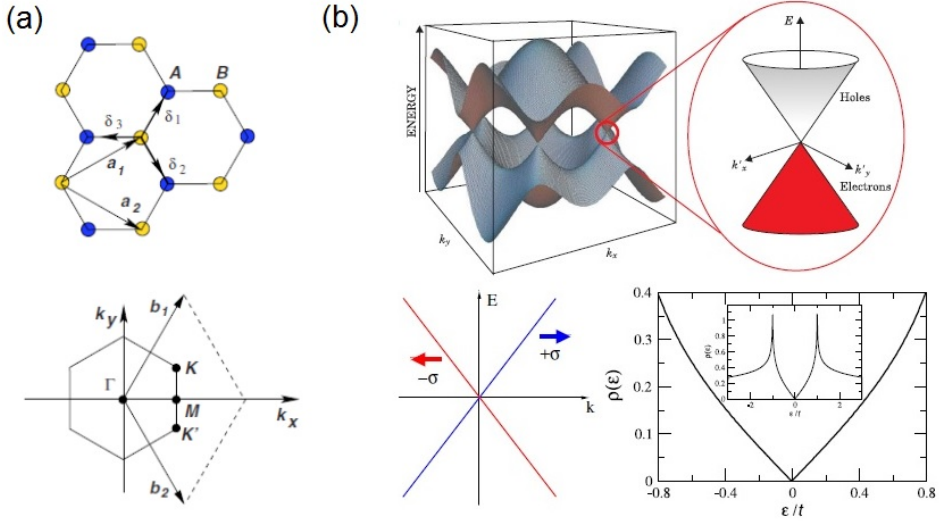


Figure 2.1: (a) Real and reciprocal lattices [1] (b) Electronic dispersion relation with close-up on the K and K' points [2].

linear dispersion relation and touch each other at a single point, the so called Dirac or charge neutrality point, on the K and K' areas of the Brillouin zone (Figure 2.1b).

$$\mathbf{H} = \hbar v_f \begin{pmatrix} 0 & q_x - iq_y \\ q_x + iq_y & 0 \end{pmatrix} = \hbar v_f \sigma \cdot \mathbf{q} \quad (2.3)$$

$$E_{\pm}(q) = \pm \hbar v_f q \quad (2.4)$$

These high symmetry points on the reciprocal space, defines most of the interesting physics of graphene. One of them is the resemblance of the electron transport to that of the massless fermions seen on the (2 + 1) Quantum Electrodynamics, with the difference that the massless Dirac fermions observed in graphene has a reduced velocity of  $v_f \sim 10^6$ , 300 times smaller than the speed of light [1]. Moreover, the identification of this particles has been proved experimentally by the observation of the anomalous quantum hall effect, which is a distinctive signature of

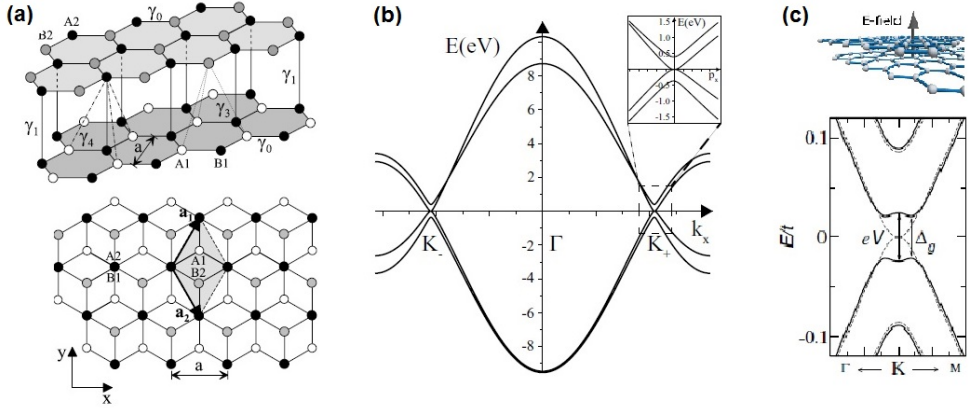


Figure 2.2: (a) Real and reciprocal lattices, (b) Electronic dispersion relation with close-up on the  $K$  and  $K'$  points [5] and (c) Band gap opening under perpendicular displacement field for AB-BLG [6]

Dirac fermions [3]. In addition to the linear dispersion relation, the joint of the bands at the Dirac point turns natural graphene into a semi-metal or a zero-gap semiconductor material with the Fermi level located in the center of the juncture, due to the electron left by the p-orbital making the bands half-filled. [4].

## 2.2 Bilayer and twisted bilayer graphene

One of the main factors that lead to the graphene discovery was the ease of isolating single layer graphene flakes by the "scotch tape method" due to the fact that graphene layers are bonded by dispersive van der Waals forces, which are hundreds of magnitude smaller to the intra-layer binding forces. Therefore, multilayer graphenes, whose appear as an intermediate systems between SLG and bulk graphite, are attractive since the coupling of stacked graphene layers makes the SLG properties to differ as the number of them changes. In this insight, bilayer graphene (BLG) has been one of the most explored graphenes, due to the close resemblance of the electronic transport to SLG, in addition to the new phenomena

observed in some of such types of systems. Moreover, apart from the number of layers, BLG can be sub-classified depending on its stacking order, where Bernal stacked bilayer graphene (or AB-BLG) and twisted bilayer graphene (tBLG) are two of the most explored BLG variants.

Bernal stacked graphene is called to the bilayer graphene where the layers are arranged so that one of the atoms from the lower layer (called B1) is directly below an atom (A2), from the upper layer. (Figure 2.2a). This atomic configuration can be also simply described by a simple crystal structure where the unit cell contains four atoms, labelled as A1, B1 and A2, B2 for the first and second layer respectively. Moreover, due to the weakly intra-layer coupling, the linear dispersion relation for conductance and valence bands of SLG transforms into a parabolic one, but leaving the zero-gap behaviour which gives rise to the massive Dirac fermions travelling at a reduced effective velocity (Figure 2.2b) [5]. Also, in contrast to natural SLG, the application of displacement field perpendicular to the BLG surface induces an asymmetry in the on-site electron energies of the top and bottom layers, leading to a band gap opening on the charge neutrality points at the K and K' areas, an interesting feature to be promising for electronic applications (Figure 2.2)[6].

On the other hand, on twisted bilayer graphene (tBLG), there exists a rotational mismatch  $\theta$  between the layers as depicted on Figure 2.3a. Consequently, the reciprocal space changes accordingly and it is necessary to redefine the basis vectors (only for commensurate cases) for each  $\theta$  angle, making impossible to unambiguously determine a single electronic spectrum for tBLG systems. However, it is possible to identify some trends on the electronic behaviour as a function of the twisting angle. For these purposes, the unit cell of tBLG can be represented as two decoupled SLG unit cells twisted by the same  $\theta$  angle where their corners, the Dirac cones at K and K', are separated by a distance  $\Delta K$ .

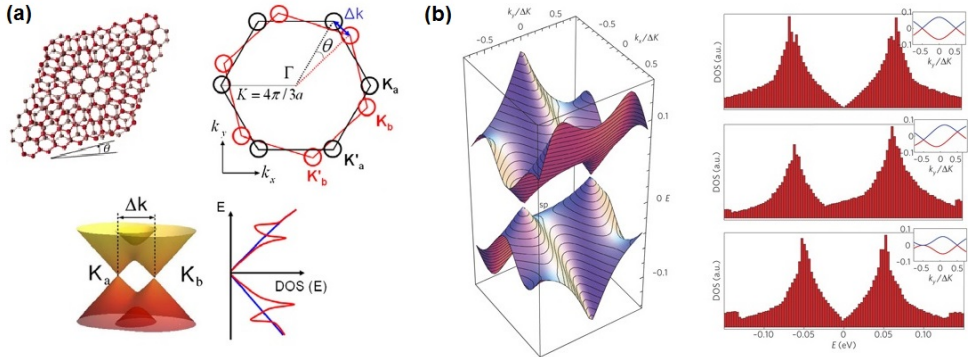


Figure 2.3: (a) Real and reciprocal lattices, electronic dispersion [7] and (b) van Hove singularities for twisted bilayer graphene [8]

proportional to the twist angle [9].

For the case of low-twist angles,  $\theta \approx 0^\circ$ ,  $\Delta K$  decreases and the Dirac cones of the layers overlaps, giving as a consequence an electronic structure resembling to that of AB-BLG. As  $\theta$  increases,  $\Delta K$  increases as well and the Dirac cones start to split until they are totally decoupled at  $\theta \approx 30^\circ$ . At this point the electronic transport is expected to behave similarly to that of two independent single graphene layers (Figure 2.3b) [10]. The behaviours of electronic transport for angles  $\theta > 30^\circ$  can be translated in the sub-thirty region cases due to the rotational symmetry of the structure, whereas detailed explanation of the electronic behaviour on intermediate angles,  $0 < \theta < 30^\circ$  is complicated due to the appearance of additional factors that might make deviate the electronic behaviour from an smooth transition between a AB-BLG system to a double SLG system [7]. However, these additional factors changes the opto-electronic properties of the material due to the appearance of new phenomena, such as the van Hove singularities (vHs) on the low energy region of the electronic spectrum (Figure 2.3b) [8], making possible the identification of the twist angle. Therefore, tBLG can still serve as an important tool for study different BLG systems as this extra degree of complexity, the

$\theta$  angle, can tune the intra-layer coupling in an suitable and controlled manner.

Finally, the particular graphene physical and electronic structure have hundreds of applications not only on the high-performance electronics field where, its extremely high mobility have been used for the production of terahertz transistors [11], but also graphene has been used in some other approaches such as: black-body light emitters due to excellent thermal conductivity [12], resistance standard due to the ease of accessibility to the fundamental constants through the quantum hall effect [13], transparent electrodes due to its low light absorption on the visible range [14] and chemical sensing due to extreme sensitivity of graphene to different environments [15], just to mention some of them.

## 2.3 Doping methods of graphene reviewed

Despite the remarkable properties of natural graphene samples, there exists a need of tailoring graphene properties in order to make them fit into some specific purposes. For this matter, doping processes have been extensively used to tune the electronic transport on graphene, since rather than simply control the Fermi energy level ( $E_F$ ), it has been possible to induce band-gap opening [18] and enhance spin-orbit coupling [19] by different means, which some of them will be discussed next.

In general, graphene doping techniques exploit the low dimensional nature of this material, where surface and interface physics play an important role in the doping process since, by simply changing the surrounding environment, it is possible to tune the electron and hole concentration. In this insight, graphene doping has been simply achieved upon exposure to different type of molecular gases, including  $O_2$  and  $H_2$ . For the first of

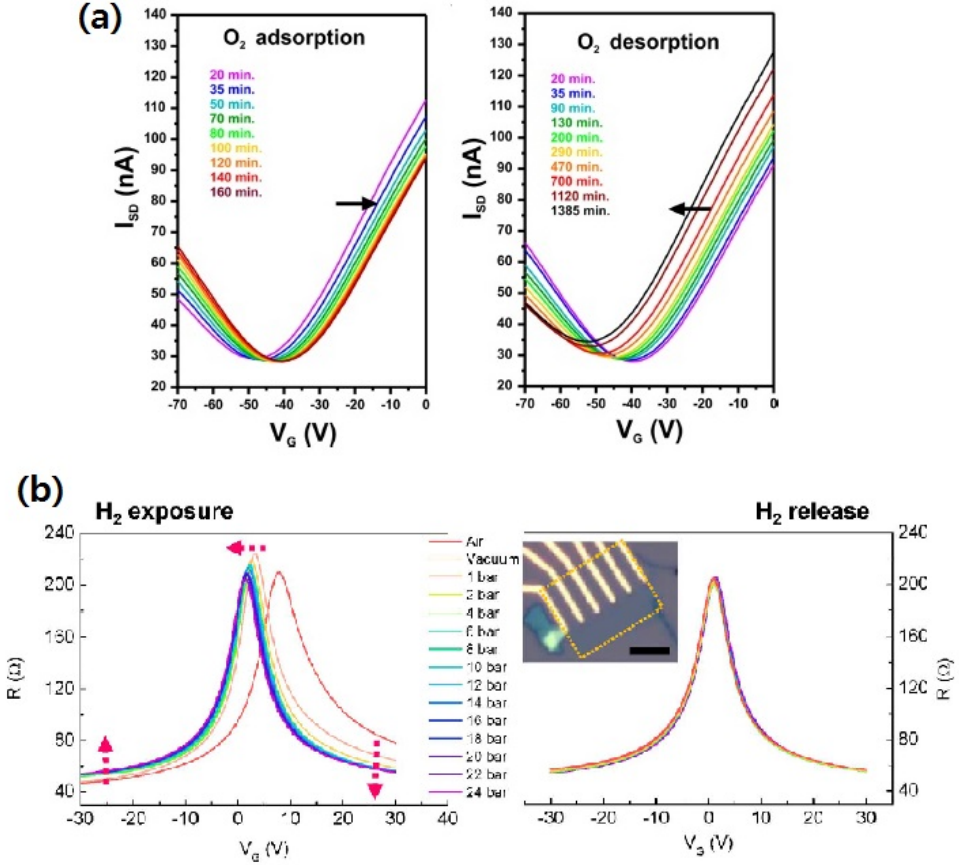


Figure 2.4: Doping of graphene samples before and after (a) O<sub>2</sub> [16] and (b) H<sub>2</sub> [17] exposure.

In the cases, it has been reported that O<sub>2</sub> produces gradual hole-doping as time develops due to the physisorption of the molecules on the graphene sample [16]. The physisorption process is explained as a small perturbation on the electronic structure of the molecules and the sample due to the interaction among them, without the formation of any chemical bonds or changes on the chemical structure. As a consequence, the doping induced by O<sub>2</sub> disappears after the normal atmospheric conditions are restored (Figure 2.4a)

On the other hand, hydrogen/graphene interactions, the ones that

this work is focused on, are reported to be governed by chemisorption, described by stronger perturbations that lead to the hybridization of orbitals and formation of covalent bonds. By exposing exfoliated graphene samples to ultra pure, high temperature, high-pressure H<sub>2</sub> atmospheres, the H<sub>2</sub> molecules dissociates at the surface of the graphene leading to the formation of C-H bonds. While one of the two H<sub>2</sub> electrons participates on the covalent bonding, the remaining electron becomes delocalized on the graphene sample, increasing the electron concentration and a consequent n-type doping effect is observed [20]. Moreover, once the process is stopped and normal conditions are restored, the sample retains its hydrogenated properties, which are observed to only disappear by thermal treatments (Figure 2.4b), reinforcing the claims about the chemisorption nature of the doping process. Therefore, due to its relative stability, graphene electron doping by means of hydrogen dissociation can be used to explore new approaches for graphene functionalization towards the incursion of this material into modern electronics.

# Bibliography

- [1] A. H. Castro Neto, F. Guinea, N. M. R. Peres, K. S. Novoselov, and A. K. Geim, *Reviews of Modern Physics* **81**, 109–162 (2009).
- [2] S. Das Sarma, S. Adam, E. H. Hwang, and E. Rossi, *Reviews of Modern Physics* **83**, 407–470 (2011).
- [3] Y. Zhang, Y.-W. Tan, H. L. Stormer, and P. Kim, *Nature* **438**, 201–204 (2005).
- [4] K. S. Novoselov, A. K. Geim, S. V. Morozov, D. Jiang, M. I. Katsnelson, I. V. Grigorieva, S. V. Dubonos, and A. A. Firsov, *Nature* **438**, 197–200 (2005).
- [5] E. McCann and M. Koshino, *Reports on Progress in Physics* **76**, 056503 (2013).
- [6] E. V. Castro, K. S. Novoselov, S. V. Morozov, N. M. R. Peres, J. M. B. L. dos Santos, J. Nilsson, F. Guinea, A. K. Geim, and A. H. C. Neto, *Physical Review Letters* **99** (2007).
- [7] K. Kim, S. Coh, L. Z. Tan, W. Regan, J. M. Yuk, E. Chatterjee, M. F. Crommie, M. L. Cohen, S. G. Louie, and A. Zettl, *Physical Review Letters* **108** (2012).
- [8] G. Li, A. Luican, J. M. B. Lopes dos Santos, A. H. Castro Neto, A. Reina, J. Kong, and E. Y. Andrei, *Nature Physics* **6**, 109–113 (2009).
- [9] A. O. Sboychakov, A. L. Rakhmanov, A. V. Rozhkov, and F. Nori, *Physical Review B* **92** (2015).

- [10] L.-J. Yin, J.-B. Qiao, W.-X. Wang, W.-J. Zuo, W. Yan, R. Xu, R.-F. Dou, J.-C. Nie, and L. He, *Physical Review B* **92** (2015).
- [11] J. Zheng, L. Wang, R. Quhe, Q. Liu, H. Li, D. Yu, W.-N. Mei, J. Shi, Z. Gao, and J. Lu, *Scientific Reports* **3** (2013).
- [12] Y. D. Kim, H. Kim, Y. Cho, J. H. Ryoo, C.-H. Park, P. Kim, Y. S. Kim, S. Lee, Y. Li, S.-N. Park, Y. Shim Yoo, D. Yoon, V. E. Dorgan, E. Pop, T. F. Heinz, J. Hone, S.-H. Chun, H. Cheong, S. W. Lee, M.-H. Bae, and Y. D. Park, *Nature Nanotechnology* **10**, 676–681 (2015).
- [13] T. Yager, A. Lartsev, K. Cedergren, R. Yakimova, V. Panchal, O. Kazakova, A. Tzalenchuk, K. H. Kim, Y. W. Park, S. Lara-Avila, and S. Kubatkin, *AIP Advances* **5**, 087134 (2015).
- [14] K. Rana, J. Singh, and J.-H. Ahn, *Journal of Materials Chemistry C* **2**, 2646 (2014).
- [15] Daniel Rodrigo, Odeta Limaj, Davide Janner, Dordaneh Etezadi, F. Javier García de Abajo, Valerio Pruneri, and Hatice Altug, *Science* **349**, 161–165 (2015).
- [16] I. Silvestre, E. A. de Moraes, A. O. Melo, L. C. Campos, A.-M. B. Goncalves, A. R. Cadore, A. S. Ferlauto, H. Chacham, M. S. C. Mazzoni, and R. G. Lacerda, *ACS Nano* **7**, 6597–6604 (2013).
- [17] B. H. Kim, S. J. Hong, S. J. Baek, H. Y. Jeong, N. Park, M. Lee, S. W. Lee, M. Park, S. W. Chu, H. S. Shin, J. Lim, J. C. Lee, Y. Jun, and Y. W. Park, *Scientific Reports* **2** (2012).
- [18] A. J. Samuels and J. D. Carey, *ACS Nano* **7**, 2790–2799 (2013).
- [19] J. Balakrishnan, G. Kok Wai Koon, M. Jaiswal, A. H. Castro Neto, and B. Özyilmaz, *Nature Physics* **9**, 284–287 (2013).
- [20] S. J. Hong, M. Park, H. Kang, M. Lee, D. Soler-Delgado, D. S. Shin, K. H. Kim, S. Kubatkin, D. H. Jeong, Y. W. Park, et al., *Applied Physics Letters* **106**, 142110 (2015).

# **Chapter 3**

## **Fabrication and experimental procedures**

In this section, all the procedures followed for the fabrication and characterization of the devices will be introduced. In order to study the modifications on the carrier transport properties of graphene upon exposure to hydrogen environments, several graphene devices were build on 3 step-basis: Growth and transfer of CVD-grown graphene into  $\text{SiO}_2$  substrates, graphene etching and electrode deposition. The crucial factors that lead to a correct fabrication of the final devices which will be explained in detail. As characterization tools, our research is based on three primary methods: Raman spectroscopy, Thermo-electric power measurement and gate-dependent I-V measurements. The configurations for these setups and the details needed for the correct execution of the measurements will be discussed as well.

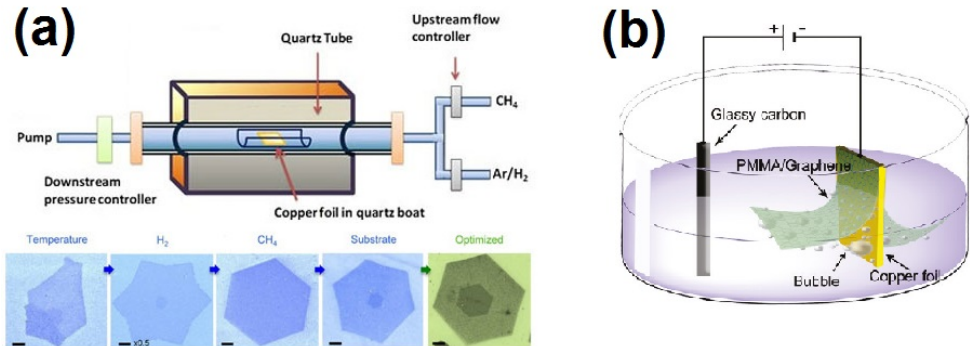


Figure 3.1: (a) CVD-process and optimization of CVD-grown tBLG flakes [5] (b) Electrochemical delamination method for graphene transfer [6]

## 3.1 Device Fabrication

### 3.1.1 CVD-Growth of twisted bilayer graphene

Chemical vapor deposition (CVD) of graphene was first reported in 2008 and 2009 [1], [2] and since then, it has been improved in order to get large areas of high-quality of graphene, where reports indicate coverage areas as large as 30 inches, enough for most of its uses on electronic applications [3]. The CVD method is based on the decomposition of a source gas (usually Methene) into carbon radicals on the top of metal substrates at high temperatures. In addition to serve as a support, metal substrates are used due to its catalytic behavior on the decomposition of the hydrocarbons and determines the graphene growth mechanism, which directly affects its quality [4].

Despite the fact that CVD-grown graphene has shown lower mobilities compared with the exfoliated graphene obtained from Highly Oriented Pyrolytic Graphite (HOPG), the CVD growth method has been extensively used due to the possibility of obtain single and multilayer graphene by modifying the growth conditions. In this manner, we exploit the advantages of the CVD method by using the Atmospheric Pressure

Chemical Vapor deposition (AP-CVD) variant in order to grow hexagonal multilayer crystalites with different stacking angle (tBLG). As it is shown on Figure 3.1a , a fine tuning of the growth conditions is necessary for obtaining spaced uniform multilayer hexagonal crystalites. During our growth process, finding a correct balance on the flow rates of the the source (Ar) and etchant ( $H_2$  ) gases, was crucial for obtaining high-quality tBLG flakes as both of them constitute the self-limiting growth process [7]. Therefore, by following the procedures described in detail elsewhere [8], we synthesized hexagonal twisted bilayer grapehene (tBLG) as follows: High purity copper foil (Alfa aesar 10950, 99.999%) was polished chemically and mechanically in prior to the growth of tBLG. The growth was performed at  $1057^\circ C$  with 500, 30-35, and 2 sccm of Ar,  $H_2$  , and  $CH_4$  (1%, balanced by 99% Ar), respectively, for 15 to 20 min. After growth, the sample cooled rapidly with 1000 and 7 sccm of Ar and  $H_2$  , respectively.

In preparation for the transferring processes, after the growth, PMMA 950k (MicroChem) was spun over one of the sides of the copper foil. The PMMA with the graphene underneath was detached from the foil by electrochemical delamination method of the copper by carefully submerging the PMMA / Graphene / Cu stack onto a 0.1 M NaOH solution in DI wa-ter [6]. Additionally, an external electrostatic potential must to be used to make the reaction favourable. Therefore, one clamp of the voltage source must be connected to some exposed copper parts on the stack, while the other clamp is directly submerged into the solution. A small potential difference at the voltage source (approximately 4 V) will be sufficient to make bubbling appear at the clamps as well as at the edges of the copper stack, indicating the progress of the reaction. As the time goes by, the PMMA film, with the graphene underneath, will be completely detached and floating on the solution where it should be picked up gently in order to keep the graphene side of the film clean. After rinsing the film on

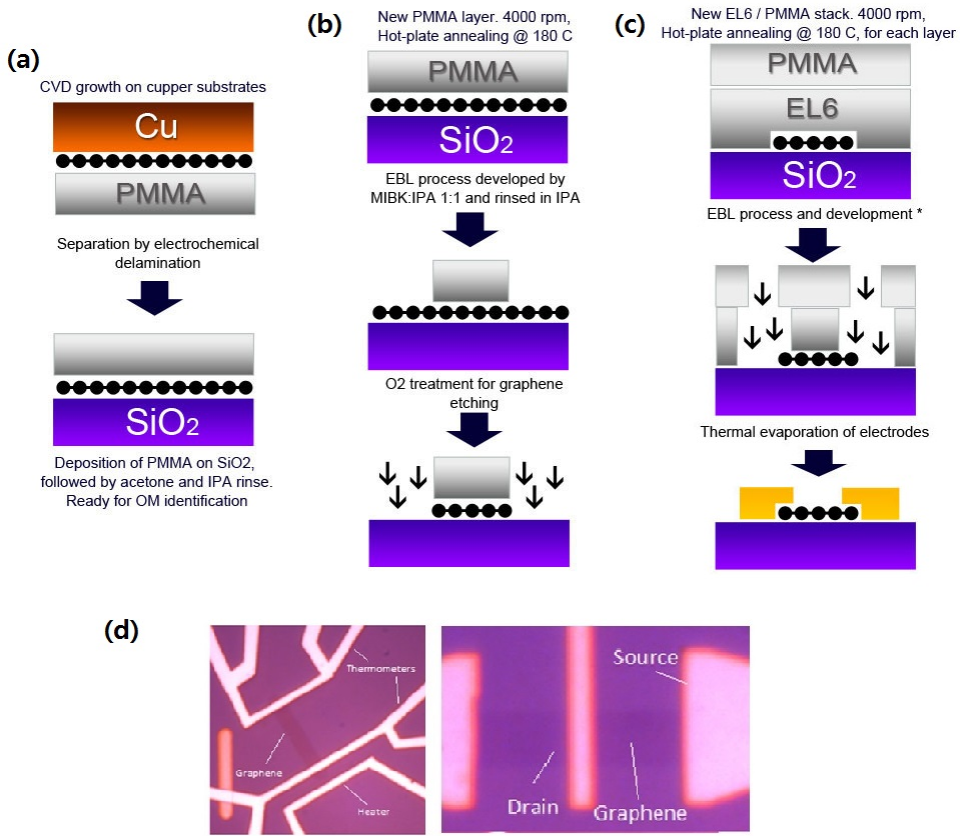


Figure 3.2: 3-step process fabrication of the graphene devices used in this work. (a) Graphene growth, transfer and optical identification, (b) graphene etching, (c) Electrode deposition and (d) Finished devices

DI water, the PMMA is placed on the top of the SiO<sub>2</sub> substrates with their backside was previously etched by BOE, in order use the exposed silicon as gate. Finally, the PMMA laying on the top of graphene can be removed easily by an acetone and IPA rinse (Figure 3.2a).

### 3.1.2 E-beam lithography

For our device preparation, two different EBL procedures were followed depending on the processing stage in course: electrode deposition or

graphene etching. For electrode deposition, a co-polymer / polymer stack consisting of EL6 and PMMA 950k (MicroChem) was spun on the top of graphene. The underneath co-polymer has higher electron-sensitivity than the PMMA, which translates it into a bigger etched area once the lithography is developed (Figure 3.2c), leaving an offset with respect of the PMMA layer. As a consequence, when the electrodes are deposited, the metals do not touch the inner walls of the cavities made on the polymer stack, making the lift-off process easier. For the graphene etching step, instead of a bilayer polymer structure, a single layer of 20 nm PPMA 950k was used. In both types of EBL process, the lithography was performed using a Tescan Mira-3 FE-SEM equipped with a NPGS system for nano-patterning at a 20 kV, with doses  $\sim 200 \mu C/cm^2$ . For developing process, a common solution MIBK:IPA 1:1, was used in which the EBL-exposed substrate was soaked for a few seconds followed by an IPA rinse.

### 3.1.3 Electrode deposition and graphene etching

The electrode deposition process consisted of a EBL process described above followed by a standard thermal evaporation to create a stack of Cr/Au of 3 nm/100 nm, respectively. The Lift-off procedure was done by immersing the samples into a acetone bath for several hours and finally rinsed with IPA. The graphene etching process was performed by O<sub>2</sub> plasma treatment following the procedures described elsewhere [9]. For masking purposes, a single layer EBL process, as described above, was used in order to select suitable rectangular areas on the tBLG flakes. After EBL and etching processes, the remaining PMMA was cleaned by an acetone and IPA rinse. Finally, an overall description of our fabrication process, including some of the details not mentioned on the main text, is shown on Figure 3.2.

## 3.2 Characterization Techniques

### 3.2.1 Raman Spectroscopy

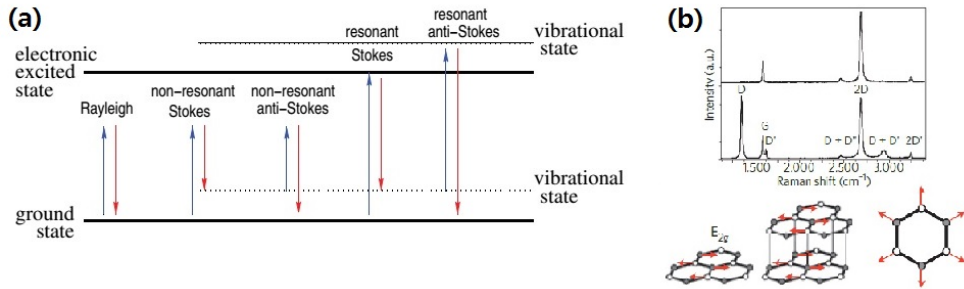


Figure 3.3: (a) Raman spectroscopy scattering processes, and the different types of light scattering. (b) Raman processes on graphene. [10]

Light-matter interactions have been useful for determining the structural and electronic properties of different materials, since as photons interacts with matter, elastic and inelastic scattering processes take place. On elastic scattering, also known as Rayleigh scattering, the energy of the out-coming photon ( $\hbar_{SC}$ ) equals that of the incoming photon ( $\hbar_L$ ). By using the energy states representation of the target to explain the elastic scattering, the photon induces a electron transition into the so-called "virtual states" which decays into the initial stationary level as the electron did not reach any higher energetic level.

In contrast to the Rayleigh scattering, inelastic scattering, also known as Raman scattering, may occur in parallel to Rayleigh scattering but at lower probability. For this process, the energies of the incident and emitted light are different, making necessary to sub-classify the Raman scattering, depending on the initial and final energetic configurations of the sample. Stokes scattering is named to the type of Raman scattering where the incoming photon is absorbed and induces an electronic transition from initial stationary state into a higher-energetic virtual state.

However, instead of returning to the initial state as the elastic case, some electrons may decay into other vibrational states with higher energies than the initial one. Therefore, the energy of the emitted photon will be decreased by an amount  $\hbar\omega_{SC} = \hbar\omega_L - \hbar\omega_\Omega$ , where  $\hbar\omega_\Omega$  is the energy difference between the initial and excited state. On the other hand, Raman Anti-stokes scattering is based on the same transition mechanism, however there exists the probability that before the photon excitation, some electrons are in higher vibrational states. In this case, the photon absorption on these electrons will excite them and make them return into the lower stationary state, emitting a photon with high energy than the incoming one by an amount:  $\hbar\omega_{SC} = \hbar\omega_L - \hbar\omega_\Omega$  as depicted on Figure 3.3a

Raman spectroscopy has its basis on these two light inelastic scattering processes, by measuring the intensity of scattered light as a function of the difference between the incident and scattered photon energy, the so-called "Raman shift" historically plotted in  $cm^{-1}$  units. Therefore, since it is possible to access to the structural and electronic information of the sample, this characterization method has been extensively used for material analysis in an non-destructive way [10].

In the case of graphene, Raman spectroscopy has been useful in determining doping [11], thickness detection [10] and strain [12]. This has been possible due to the high sensibility of graphene to external factors, where the most of the analysis are based on the following peaks of its spectrum: The G-band ( $\sim 1580 cm^{-1}$ ) which is related to the double degenerate zone center  $E_{2g}$  mode. The D-band ( $\sim 1350 cm^{-1}$ ), related as a breathing mode of the  $A_{1g}$  symmetry and which presence is attributed to disordered samples. The 2D-band ( $\sim 2700 cm^{-1}$ ), originated from a second-order process, involving two iTO phonons near the K point [13], and the R-R' peaks which are signature of the existence of twisting angle

between layers [5].

For our research, Raman spectroscopy was used for two main purposes: First, to detect twisted angle on bilayer structures, this characterization was done on all devices. And second, to verify and support our observations on the hydrogenation processes that were mainly characterized by means of electrical measurements. All our Raman characterization measurements were performed using a LabRam 300 by JY-Horiba spectrometer, with a wavelength of 532 nm and a laser power of 0.2 mW in order to avoid any damage of the devices.

### 3.2.2 Electrical measurements

Since the early beginnings of the graphene research, gated electrical measurements have been selected as the preferred characterization method, not only to its relative ease of execution, but also because its attributes give important information about the electronic structure, due to the possibility of tuning the carrier concentration and evidently the Fermi level of the graphene devices. For this reason, we based our electrical characterization in 2 types of gated measurements. Gate-dependent I-V measurements (Also known as transfer curve method) and Thermo-electric power measurements.

#### Gate-dependent I-V measurements

Figure 3.4a shows the schematic of the simplest of our characterization methods and a common transfer curve for a field effect transistor (FET) configuration where pristine graphene acts as a channel. The peculiar form of the pristine graphene transfer curve reveals the linear dispersion nature of the low-energy region, where the Dirac point on the momentum space is translated onto a minimum conductance point (also known as

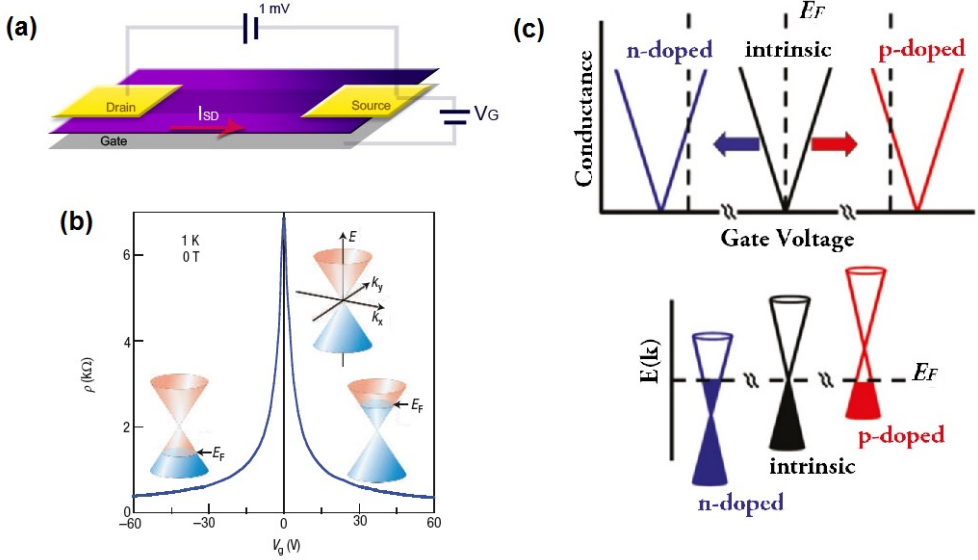


Figure 3.4: (a) Schematic of graphene FET showing the potential bias configuration, (b) Transfer curve of pristine single layer graphene denoted as a graph of  $V_G$ -Resistance or  $V_G$ -Conductance [14]. (c) Electron and hole doping representation on the energy dispersion diagram and the transfer curves

$V_{CNP}$ ) at  $V_G = 0$ . Due to the fact that the potential difference  $V_G$  can be translated into an effective induced carrier density inside the sample by:

$$n_{ind} = \frac{C_G}{e}(V_G - V_{CNP}) \quad (3.1)$$

where  $C_G$ ,  $e$ ,  $V_G$  and  $V_{Dirac}$  are the capacitance per unit area, electron charge, gate voltage and the minimum conductance voltage or CNP, respectively, it is possible to control the population of the low-energy levels of graphene and as a consequence monitor electronic changes on our samples in on this region [14].

One of the most characteristic phenomena observed on the transfer curves is the doping effect. On pristine graphene, the Fermi energy ( $E_F$ ) is placed right on the Dirac point at the 0 eV. However, whenever there

exists additional holes or electrons, the  $E_F$  is shifted upwards towards the conduction band or downwards towards the valance band. In our transfer curves, this is directly reflected by a shift on the  $V_{CNP}$  towards positive values in case of hole doping and towards negative values in case of electron doping, as it can be depicted on Figure 3.4c.

In our measurements, the gate-dependent I-V curves were measured frequently, in order to study the temporal evolution of the hydrogen effects on the CVD-grown hexagonal twisted bilayer graphene devices by using an 4200-SCS Keithley Parameter Analyzer. All the measurements were performed on a two probe, steady-state configuration (DC characterization) with a  $V_{DS} < 1mV$  to avoid damages on our samples.

### **Thermoelectric power measurements**

The Seebeck coefficient ( $S$ ), also know as Thermo-electric power (TEP), represents the relation between the temperature gradient  $\nabla T$  and the electric field  $E$  across the sample in an open-circuit configuration such as  $\vec{E} = S \nabla \vec{T}$ . When a material is subject to heating, the main carriers inside of it respond to the temperature gradient moving from the hot to the cold region. This charge movement produces an electric field, which retards the thermal diffusion until it reaches an equilibrium configuration leading a zero net carrier flow.

Therefore, by measuring the potential drop  $\Delta V$  on the hot and cold regions as depicted on Figure 4.5a, it is possible to specify  $S$ , which is positive ( $S > 0$ ) or negative ( $S < 0$ ) when the main carriers on the sample are holes or electrons, respectively. Moreover, in addition to the potential measurement, the hot and cold electrodes are used to measure the temperature gradient by establishing the relation between the resistance of the electrode as function of the temperature as depicted on Figure 3.5b.

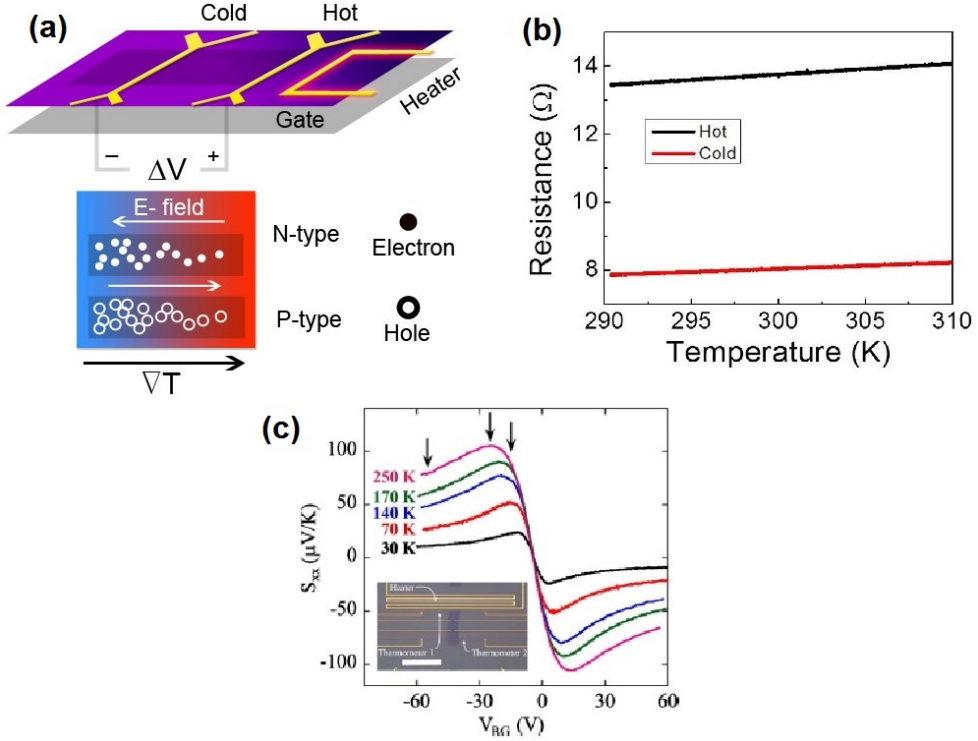


Figure 3.5: (a) Schematic showing principle of operation of thermoelectric power measurement (b) Calibration curve for the set of thermometers and (c) graphene Seebeck coefficient as a function of gate-voltage [15]

For the case of graphene, thermoelectric power, in conjunction with the gating mechanism, has been used to explore the carrier transport inside the material. Figure 4.5c, shows a particular curve of these measurements done on pristine graphene [15]. As it is expected from the transfer curve measurements, the Seebeck coefficient have a transition from positive to negative values, close to the  $V_G = 0$ , indicating the change on the main carrier from holes to electrons. Furthermore, it has been demonstrated that graphene, as well as carbon nanotubes, follow the semi-classical Mott's relation, reinforcing the usefulness of the Boltz-

mann transport formalism [16]:

$$S = -\frac{\pi^2 k_B^2 T}{3|e|} \frac{1}{\sigma} \frac{d\sigma}{dV_G} \frac{dV_G}{dE} \Big|_{E=E_F} \quad (3.2)$$

where  $\sigma$ ,  $k_B$ ,  $T$  and  $V_G$  are the conductivity, Boltzmann constant, temperature and gate voltage, respectively.

In our measurements, the TEP where performed on hydrogenated and pristine graphene conditions in order to support our results obtained by the transfer curve method. In all our experiments, TEP was performed an standard steady-state technique with a temperature gradient such that  $\Delta T \ll T$ .

### 3.3 Hydrogenation of Graphene devices

As a conclusion for the current chapter, a general summary of the fabrication and experimental procedures is presented for further references. Once the growth and transfer procedures of our CVD hexagonal twisted bilayer graphene were performed, the  $\text{SiO}_2$  substrates were inspected by optical microscopy to select suitable crystallites, which its twisted nature was cross verified by Raman spectroscopy measurements prior any hydrogen treatment. Further fabrication processes were executed to the make graphene devices on the field-effect transistor or thermo-electric power configuration.

To study the effects of hydrogen on hexagonal twisted bilayer graphene devices, a high-vacuum / high-pressure chamber, depicted on Figure 3.6, was used, where all the electrical characterization measurements were performed without exposing the sample to atmosphere conditions. Upon the fabrication, the graphene devices were introduced into the chamber

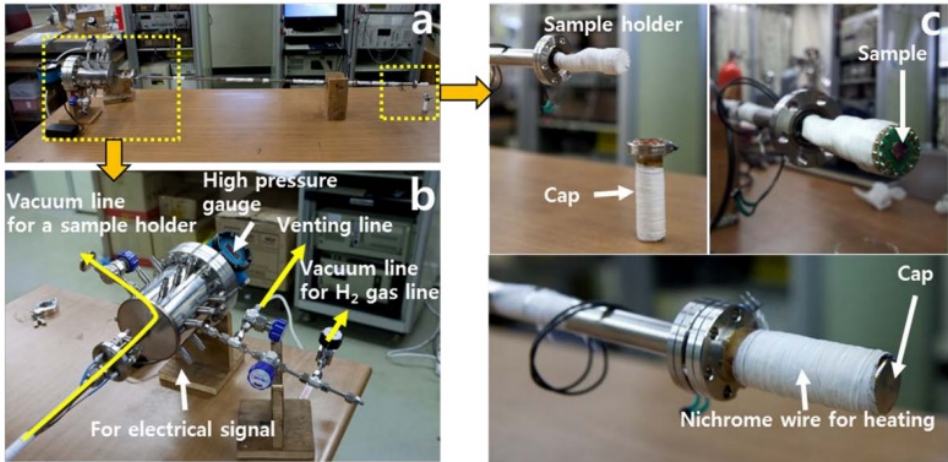


Figure 3.6: Probe for cryostat and high  $H_2$  pressure. a, Full-length photograph of the probe b, Head of the probe consisted of two vacuum lines for a sample holder and  $H_2$  gas line, venting line, high pressure gauge, and BNC type coaxial connector to sense an electrical signal. c, The sample holder is composed of a cap with nichrome wire for heating, Cu gasket, and chip holder made of Teflon [17]

and subjected to a thermal annealing procedure in high vacuum at 350 K, in order to remove some of the impurities left by the previous processing steps. The main goal of the annealing procedure was to restore the pristine conditions of the graphene and lasted for several hours until the  $V_{CNP}$  did not show any further shift. The electrical measurements done under this set of conditions represent our pristine or zero-minute exposure data. After the annealing procedure, the exposure stage started by flowing  $H_2$ , 99.9999%, pure into the chamber until the pressure reached a base value of 11 bar, preserving the temperature at 350 K. Following the exposure stage, the measurement stage was performed by keeping the base pressure steady and decreasing the temperature to 300 K. Here, the transfer curve or the Seebeck coefficient was recorded. Several exposure times on the same sample were explored by switching between exposure (300 K) and measurement stage (350 K) accordingly. The sum of the time of the subsequent exposure stages is the one that is considered in

our time-dependent studies.

Finally, when Raman spectroscopy is done on post-H<sub>2</sub> treated samples, the samples are taken out from the chamber but our graphene samples are expected to remain the hydrogenated properties due to the nature of the graphene/H<sub>2</sub> interaction, described as a chemisorption process [9].

# Bibliography

- [1] Q. Yu, J. Lian, S. Siriponglert, H. Li, Y. P. Chen, and S.-S. Pei, Applied Physics Letters **93**, 113103 (2008).
- [2] Xuesong Li, Weiwei Cai, Jinho An, Seyoung Kim, Junghyo Nah, Dongxing Yang, and Richard Piner, Science **324**, 1312–1314 (2009).
- [3] S. Bae, H. Kim, Y. Lee, X. Xu, J.-S. Park, Y. Zheng, J. Balakrishnan, T. Lei, H. Ri Kim, Y. I. Song, Y.-J. Kim, K. S. Kim, B. Özyilmaz, J.-H. Ahn, B. H. Hong, and S. Iijima, Nature Nanotechnology **5**, 574–578 (2010).
- [4] Y. Zhang, L. Zhang, and C. Zhou, Accounts of Chemical Research **46**, 2329–2339 (2013).
- [5] C.-C. Lu, Y.-C. Lin, Z. Liu, C.-H. Yeh, K. Suenaga, and P.-W. Chiu, ACS Nano **7**, 2587–2594 (2013).
- [6] Y. Wang, Y. Zheng, X. Xu, E. Dubuisson, Q. Bao, J. Lu, and K. P. Loh, ACS Nano **5**, 9927–9933 (2011).
- [7] A. W. Robertson and J. H. Warner, Nano Letters **11**, 1182–1189 (2011).
- [8] S. J. Hong, “Electrical properties of modified graphene via doping and stacking”, PhD thesis (Seoul National Univiersity, Dec. 2015).
- [9] S. J. Hong, M. Park, H. Kang, M. Lee, D. Soler-Delgado, D. S. Shin, K. H. Kim, S. Kubatkin, D. H. Jeong, Y. W. Park, et al., Applied Physics Letters **106**, 142110 (2015).

- [10] A. C. Ferrari, J. C. Meyer, V. Scardaci, C. Casiraghi, M. Lazzeri, F. Mauri, S. Piscanec, D. Jiang, K. S. Novoselov, S. Roth, and A. K. Geim, Physical Review Letters **97** (2006).
- [11] A. Das, B. Chakraborty, S. Piscanec, S. Pisana, A. K. Sood, and A. C. Ferrari, Physical Review B **79** (2009).
- [12] O. Frank, G. Tsoukleri, J. Parthenios, K. Papagelis, I. Riaz, R. Jalil, K. S. Novoselov, and C. Galotis, ACS Nano **4**, 3131–3138 (2010).
- [13] L. Malard, M. Pimenta, G. Dresselhaus, and M. Dresselhaus, Physics Reports **473**, 51–87 (2009).
- [14] A. K. Geim and K. S. Novoselov, Nature Materials, 183–191 (2007).
- [15] S.-G. Nam, D.-K. Ki, and H.-J. Lee, Physical Review B **82** (2010).
- [16] Y. M. Zuev, W. Chang, and P. Kim, Physical Review Letters **102** (2009).
- [17] B. H. Kim, S. J. Hong, S. J. Baek, H. Y. Jeong, N. Park, M. Lee, S. W. Lee, M. Park, S. W. Chu, H. S. Shin, J. Lim, J. C. Lee, Y. Jun, and Y. W. Park, Scientific Reports **2** (2012).

# **Chapter 4**

## **N-type doping on CVD-grown twisted bilayer graphene devices by hydrogen adsorption**

### **4.1 Identification of CVD-grown twisted bi-layer graphene**

Among the first stages of fabrication processes of our graphene devices, the identification of the twist angle  $\theta$  of our CVD grown tBLG flakes stands out, as by classifying BLG with different stacking order, we would be able to appreciate the modifications on the carrier transport upon hydrogen exposure and put them into perspective with those previously reported on the literature. Therefore, as it has been stated before, this  $\theta$  identification procedure consisted on a cross-verification between optical microscopy and Raman spectroscopy.

By taking advantage of the high contrast of the  $\text{SiO}_2$  / graphene in-

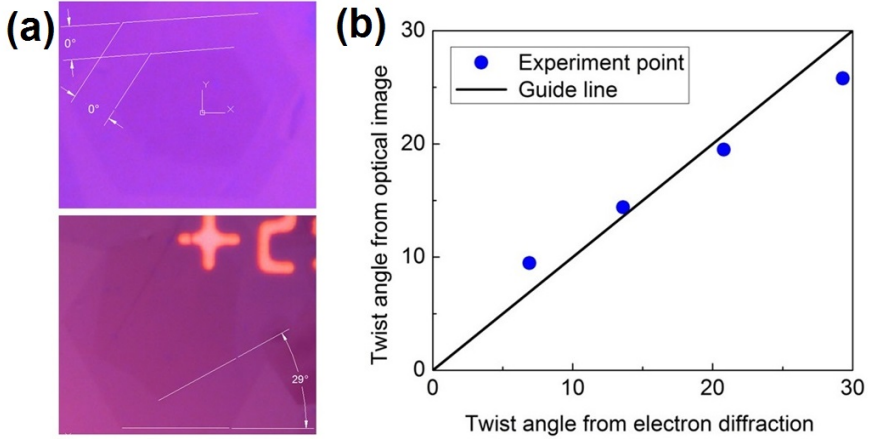


Figure 4.1: (a) Twist angle of tBLG flakes estimated by optical microscopy, (b) Correspondance of  $\theta$  between optical microscopy and TEM [1]

terface [2], we selected tBLG flakes as depicted on Figure 4.1a. The fine tuning on our growth conditions made possible to produce hexagonal shapes on the bottom and top layer of our bilayer stacks, whose edges were perfectly observed by the color change on the shadows. A previous study on these systems have related the twisting angle measured by the flake edges under optical microscopy and transmission electron microscopy, with a good agreement between the two values as shown on Figure 4.1b [1]. Therefore, on large twisted angles ( $\theta \gg 0^\circ$  but  $\theta < 30^\circ$ , due to the rotational symmetry of the system), single optical microscopy identification was used to estimate the twisted angle between the layers. However, despite the fact that optical identification gives a good estimate for large twisting angles, this method becomes uncertain for small twisting angles ( $\theta \approx 0^\circ$  and  $\theta \approx 30^\circ$ ), requiring Raman spectroscopy as a supportive method.

Figure 4.2a shows the Raman spectra of the three selected devices with small twisted angles. In agreement to what it was previously described on the last chapter, our spectra contains 4 important features:

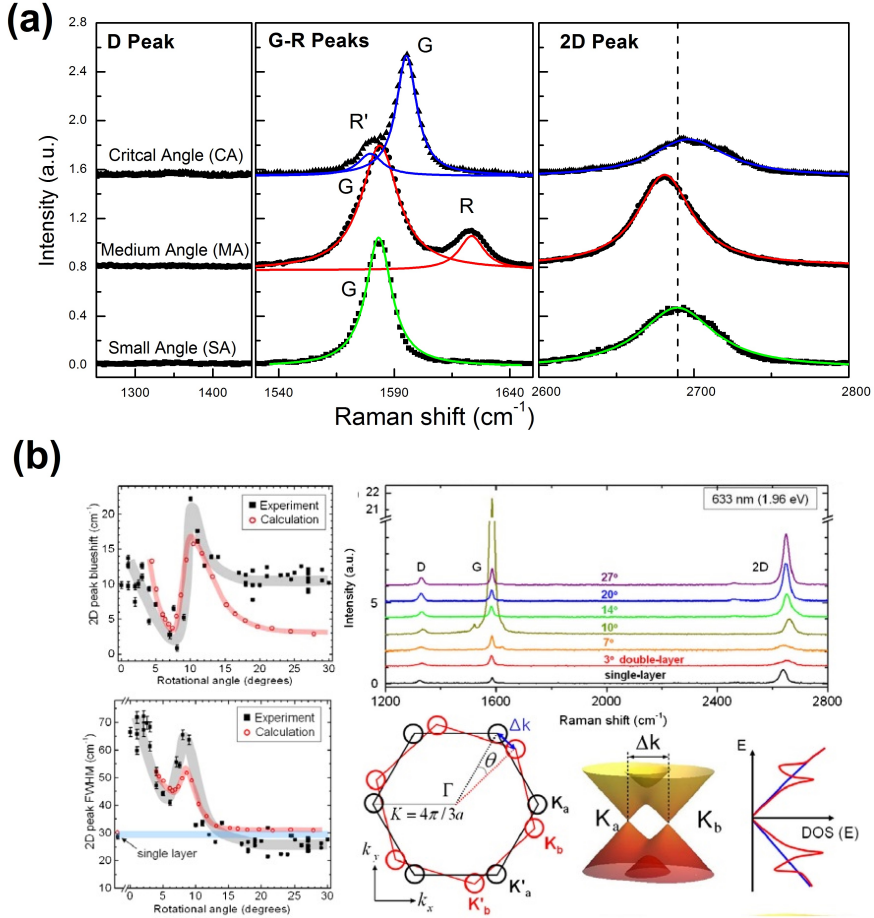


Figure 4.2: (a) Raman spectroscopy of bilayer graphene devices with different stacking angles. Colored lines represents the fitted values reported on Table 4.1. (b) Behaviour of G and 2D bands as a function of  $\theta$  [3]

D, G, 2D and R-R' bands. The G and 2D peaks appears on all the graphene systems and their sensitivity to the number of layers, stacking order, doping and strain will help us to identify our samples and recognize some important features induced by the hydrogenation process. For the specific case of rotational mismatched graphenes, by tracking the evolution of the G and 2D peak, it is possible to estimate the smallest twist angles of our samples [3].

	<b>Pos (2D)</b> ( $cm^{-1}$ )	<b>FWHM (2D)</b> ( $cm^{-1}$ )	<b>I(G)/I(2D)</b> ( <i>a.u.</i> )
<b>SA</b>	2689.36	58.684	1.037
<b>MA</b>	2681.17	41.978	1.360
<b>CA</b>	2696.45	59.442	2.436

Table 4.1: Fitted values of G and 2D peaks for small angle samples. SA, MA and CA stands for small, medium and critical angle, respectively

Twisted bilayer graphene can be defined as a two non-interacting SLG with a rotational mismatch  $\theta$  between them. This angle of rotation is also reflected on the momentum space, as tBLG can be represented by two rotated SLG Brillouin zones by the same  $\theta$  angle. At sufficient small  $\theta$ , there exists some regions on the momentum space where the Dirac cones of the top and bottom layers overlap, modifying the non-interacting density of states (DOS) and giving rise to the van Hove singularities [4]. For a given  $E_L$ , it is possible to calculate the so-called critical angle value  $\theta_c$ , the twisting angle at which the laser wavelength matches the energy difference between the vHS of the valence and conduction band:

$$\theta_c = \frac{3aE_L}{\hbar v_f 4\pi} \quad \theta_c \approx 12^\circ \quad (4.1)$$

$$E_L = 2.33eV \quad (4.2)$$

where  $a$ ,  $\hbar$ ,  $v_f$ , are the monolayer graphene lattice constant, the reduced Planck constant, and the Fermi velocity ( $10^6$ ), respectively. Therefore, it is expected that for a given  $E_L$ , as  $\theta \rightarrow \theta_c$ , the Raman spectra will change dramatically as inter-layer interaction becomes stronger. As it can be seen on Figure 4.2b, the position and the FWHM have a non-monotonical behaviour as a function of  $\theta$ , with minimum between  $0^\circ$  and  $\theta_c$ . Our samples have the same trend as indicated on Table 4.1, which shows some of the fitting data for the three small angle devices, where the medium angle (MA) sample shows the lowest Pos (2D) and FWHM (2D) from the set. Moreover, the intensity ratio I(G)/I(2D) increases with the

twist angle from 1.037 of the small angle sample (SA) to 2.436 of the critical angle sample (CA), indicating that indeed, the SA, MA and the CA samples can be sorted in an increasing fashion on the twisting angle.

Finally, in addition to characteristic behaviour on the G and 2D band, the appearance of the R-R' peaks on some of the Raman spectra reinforces the correct classification given to the three selected samples. The origins of the R-R' peak bands are related with an intra-valley scattering of the electrons, which is activated by a superlattice wave-vector formed by the twisted structure and it is only visible at small twisted angles [5]. As the twisting angle develops, a satellite peak on the Raman spectrum appears to the right of the G-band at smaller angles (MA sample) and ends up vanishing on the left side of the G-peak as  $\theta$  goes near to the critical value (CA sample). For angles near zero, the Raman spectrum resembles to that of the AB-SLG and as a consequence, no R-R' peaks are noted on our measurements (SA sample). [6]

## 4.2 Transfer curves of graphene devices under hydrogen exposure

Figure 4.3 shows the transfer curves of the four devices subject to hydrogen exposure: the three devices with angles lower than  $\theta_c$  characterized by Raman spectroscopy (label as small, medium and critical for SA, MA and CA, respectively) and a fourth device with twisting angle  $\theta > \theta_c$ . For each sample, the final exposure time was around 40 hours with subsequent measurements stages in between.

There are several features on the transfer curve that are shared by all the samples regardless of the twist angle: First, the pristine condition showed a prominent shift of the  $V_{CNP}$  towards the positive

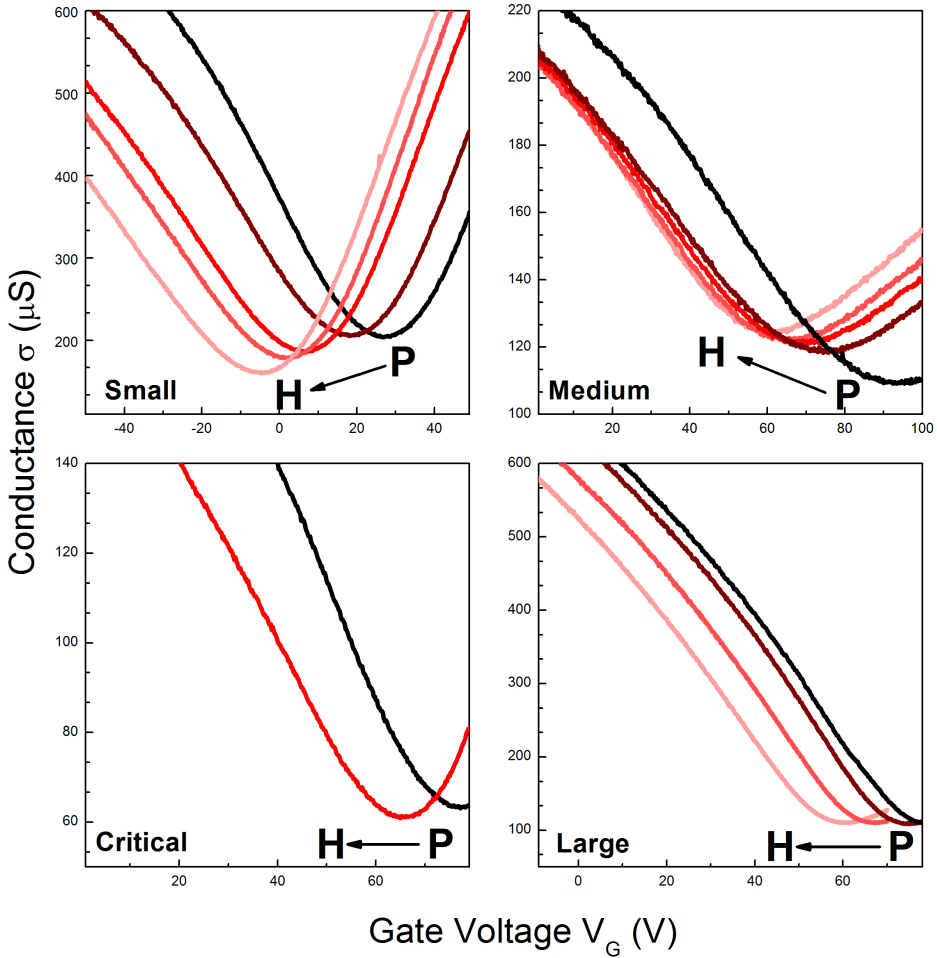


Figure 4.3: Transfer curves of all our devices as a function of time. The arrow indicates the time transient starting from the transfer curve under pristine condition (P) to the transfer curve with highest exposed sample (H). The color gradient also remarks this trend.

$V_G$  values. Whereas the reason of this hole doping behaviour cannot be uniquely determined, we would like to address two possible causes: (1) the unavoidable polymer contamination during the transfer and fabrication of the device and (2) the inclusion of external dopants due to the exposure to atmospheric conditions. Second, Upon hydrogen exposure, there is a shift on the  $V_{\text{CNP}}$  towards the negative  $V_G$  region. This

behaviour clearly demonstrate electron doping, induced by hydrogen adsorption onto the CVD-grown tBLG devices as suggested by complementary Raman spectroscopy characterization. Third, There are no insights of band gap opening. This is consistent with previously reported research on AB-stacked BLG samples [7] and finally, as exposure time develops, there occurs two phenomena in parallel: the  $V_{CNP}$  moves towards negative values exponentially and there exists an asymmetric evolution of the transfer curves. These features reveals details on the chemisorption process of hydrogen on graphene, as well as hole and electron transport through the sample.

### 4.3 Raman spectroscopy of hydrogenated tBLG

In order to support the electron doping observations on the transfer curves, Raman spectroscopy was performed on the small angle sample after hydrogen exposure (Figure 4.4a) and the fitted values are shown on Table 4.2. As a first insight, despite both G and 2D peaks show a blueshift, the 2D-peak does it in a more prominent way as  $\Delta\omega_{2D} \sim 3\text{ cm}^{-1}$  compared to the  $\Delta\omega_G = 0.38\text{ cm}^{-1}$  of the G-band.

This behaviour is better supported by using the transfer curve mea-

	Pristine	$H_2$ Exposure
$\omega_G$	$1583.26\text{ cm}^{-1}$	$1583.64\text{ cm}^{-1}$
$\Gamma_G$	$12.99\text{ cm}^{-1}$	$14.14\text{ cm}^{-1}$
$\omega_{2D(1A)}$	$2683.29\text{ cm}^{-1}$	$2686.66\text{ cm}^{-1}$
$\omega_{2D(2A)}$	$2706.80\text{ cm}^{-1}$	$2709.87\text{ cm}^{-1}$

Table 4.2: Fitted values of G and 2D peaks, before and after hydrogen exposure

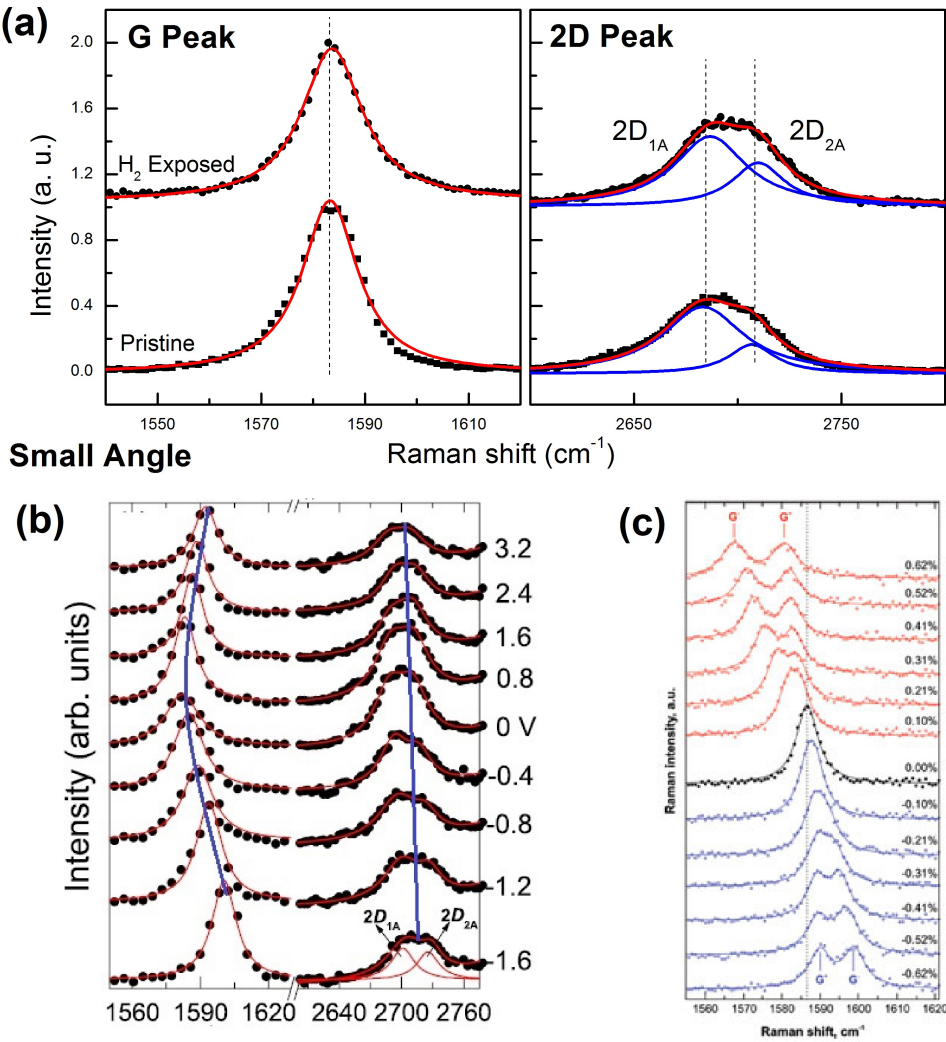


Figure 4.4: (a) Raman spectroscopy small angle sample before and after hydrogen exposure. The peak fitting information is available on Table 4.2, (b) Raman spectroscopy of BLG as a function of gating voltage, adapted from [8],(c) Raman spectroscopy of compressed graphene [9]

surments which show that our small angle device was initially hole-doped with a large positive  $V_{\text{CNP}}$  value, and it ended up on the negative  $V_G$  region, with  $V_{\text{CNP}}$  quite close to zero. In terms of the Raman spectroscopy, a pure transition of highly hole-doped to a lightly electron-doped state

would be translated into a redshift on the G-peak, with no shift on the 2D-peak as depicted on Figure 4.4b [8]. However, considering that H<sub>2</sub> dissociates on the surface of graphene, electron doping is accompanied by certain lattice compression due to the formation of the C-H bonding as it has been revealed by transmission electron microscopy [10]. Different research studies has shown that Raman spectroscopy of pure compressible strain (Figure 4.4c) blueshifts the G and the 2D peaks as a function of the strain percentage [9]. Therefore, the difference on the blueshifts between the G and 2D peak can be explained as a competition between electron doping resulting from the delocalized electron of the H<sub>2</sub> pair and lattice strain induced by the C-H formation [11]. As a result, the net effect of these both processes annihilate for the G-peak, giving as a result a smaller blueshift than the case of the 2D-peak, where the two processes enhance the shift towards the positive values of the Raman spectrum.

## 4.4 TEP measurements of graphene device under hydrogen exposure

In addition to the post-hydrogenation Raman spectroscopy measurements, the Seebeck coefficient of the critical degree angle was measured as depicted on Figure 4.5. It is important to notice that the measurements were stopped at 80 V in order to keep the integrity of the samples. Although the swept V<sub>G</sub> region was not large enough to cover that of electron transport, our measurements are still sufficient to recognize the features that supports our observations of electron doping.

At first insight, the Seebeck coefficient curve has all the features as previously described for graphene systems before and after hydrogenation [12]. However, there is a shift on the point where S = 0 towards a negative V<sub>G</sub> value after hydrogen exposure. As it has been discussed be-

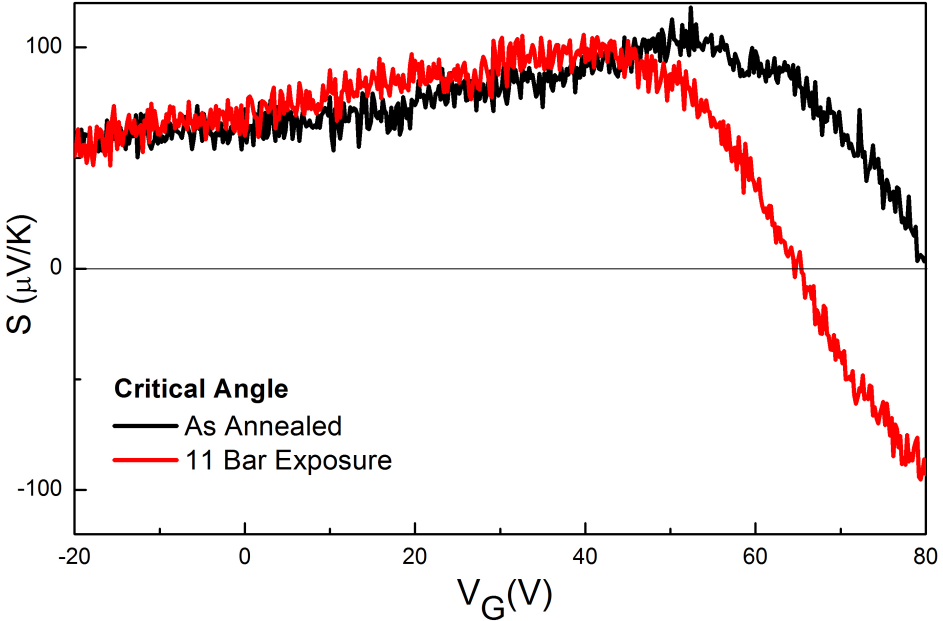


Figure 4.5: Seebeck coefficient for the critical angle sample before and after hydrogen exposure

fore, this transition point on the Seebeck coefficient indicates the change from holes to electrons as the main carriers of the sample and agrees with the shift on the  $V_{CNP}$  from 65.81 V to 77.40 V seen on the transfer curves measurements.

Furthermore, the maximum Seebeck coefficient value on the hole regime rounds on the  $120 \mu V/K$  which is consistent with those previously values measured on BLG samples and it is not enhanced nor decreased after hydrogenation. As for the characteristics far from the Dirac point, the tendency of  $S \rightarrow 0$  as  $V_G \rightarrow -\infty$  in pristine and hydrogenated cases is preserved. Since  $S$  can be interpreted as the entropy per carrier, this indicates the existence of a degenerate state in the highly doped limit, consistent in both measurements [13]. Therefore, because of the conservation on the shape and characteristics on the Seebeck coefficient

measurements upon H<sub>2</sub> treatments, we can conclude that upon exposure to the molecular hydrogen environment, the n-type doping process in twisted BLG graphene does not change prominently its electronic structure, in agreement with similar studies done on SLG [11].

## 4.5 Development of device features as hydrogen exposure

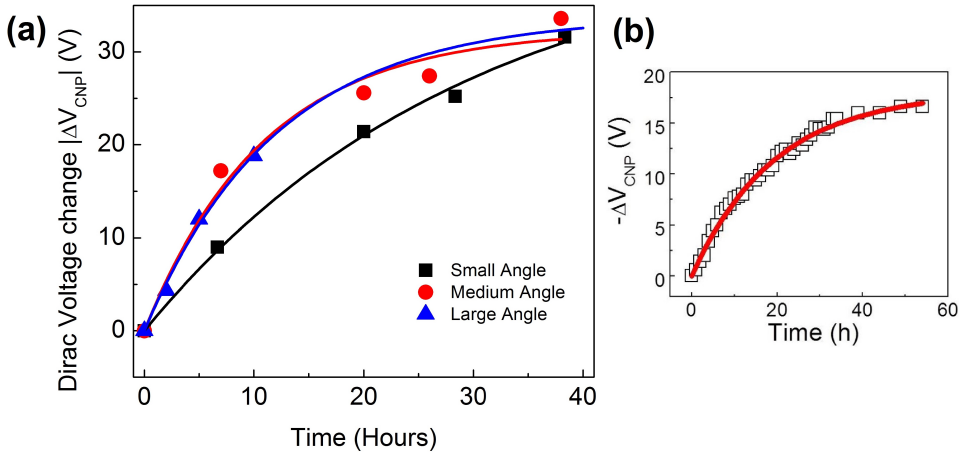


Figure 4.6: (a)  $V_{CNP}$  for different twisted angles as a function of time. The fitted exponential functions on the  $V_{CNP}$  plot correspond to the first-order absorption process (b) First-order adsorption process of H<sub>2</sub> on a BLG / h-BN device [7]

Lastly, in spite of obtaining further information to describe our transfer curves (Figure 3.4), the  $V_{CNP}$  and the carrier mobilities are studied as a function of time exposure. Figure 4.6a shows the  $V_{CNP}$  difference with respect of the pristine condition, as a function of time. ( $|\Delta V_{CNP}|(t) = |V_{CNP}^{Pristine} - V_{CNP}(t)|$ ) It is clearly seen that, for all the twisting angles,  $\Delta V_{CNP}$  can be perfectly fitted by an exponential func-

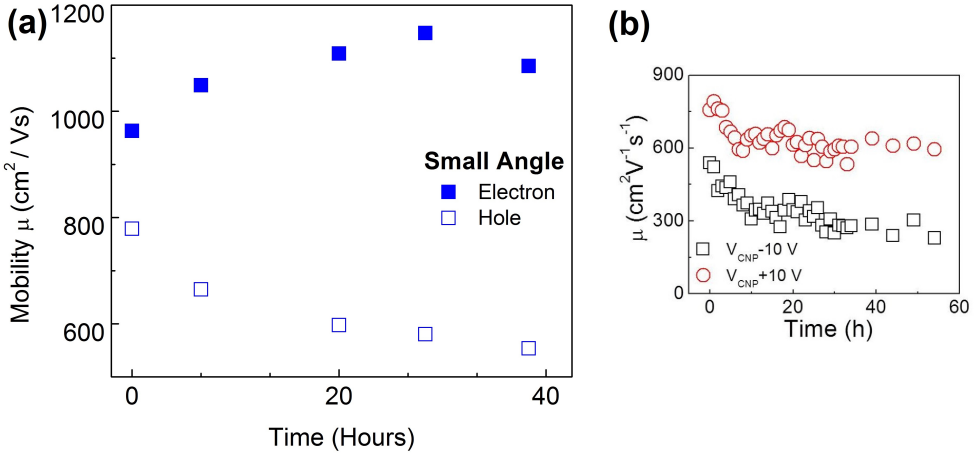


Figure 4.7: Evolution of carrier mobility as a H<sub>2</sub> time exposure for (a) Our sample tBLG / SiO<sub>2</sub> (b) BLG / h-BN device [7]

tion:

$$\Delta V_{CNP} = \Delta V_{CNP0}(1 - e^{-kt}) \quad (4.3)$$

Due to the fact that the  $\Delta V_{CNP}$  can be related with the impurity carrier density by  $n_{imp} = (C_G/e)|\Delta V_{CNP}|$ , the exponential behaviour on the  $V_{CNP}$  as a function of time represents a first order adsorption model of the hydrogen molecules onto the graphene surface [14]. Moreover, this adsorption model has been observed on exfoliated BLG / h-BN structure (Figure 4.6b), where substrate intercalation of hydrogen can be mitigated [7], indicating that the hydrogen dissociation at high temperature follows the same path and it is intrinsic of bilayer graphene samples, regardless of the extra internal degree of complexity  $\theta$

The other interesting feature on the transfer curve is the asymmetric evolution of the electrons and hole mobilities as a function of time exposure (Figure 4.7a). The mobilities were extracted from the transfer curves by using the following relation:

$$\mu_c = \frac{1}{C_G} \frac{d\sigma}{dV_G} \quad (4.4)$$

where  $\mu$  is the mobility of holes ( $c = h$ ) or electrons ( $c = e$ ),  $C_G = 115 \text{ aF}/\mu^2$  is the capacitance per unit area and  $\sigma$  is the conductance of the sample. The derivative term was taken from the slope of the linear region at the left or right of the charge neutrality point for holes or electrons, respectively [15]. Figure 4.7a contains the graph described above, showing that the electron mobility increases as a function of time, while the hole mobility does the opposite. This asymmetric evolution of the mobilities is better understood if we consider the same BLG / h-BN studies as before. Due to the fact that the  $\text{SiO}_2$  impurities are suppressed by the h-BN substrate, the BLG on the top does not suffer of any other scattering mechanism rather than the hydrogen impurities and those coming from the graphene itself. Consequently, there exists a pure decrease on the electron and hole mobilities (Figure 4.7b) due to the fact that the dissociated hydrogen has been catalogued as a short-range scatterer [16].

However, when graphene is placed over bare  $\text{SiO}_2$ , its roughness, impurities and dangling bonds can act as a scatterers centers increasing the electron mobility and hindering the pure effects that the hydrogen adsorption has on graphene. The mobility asymmetry caused by the substrate has been observed on exfoliated BLG upon hydrogen [10] and oxygen [14] exposure. Therefore, while hydrogen adsorption on CVD-grown tBLG might act as a short-range scatterer as well, there is a need of reproduce further experiments by using high-quality substrates, to reduce the external perturbations, and different stacking angles  $\theta$ , to explore the interlayer interactions and generalize the results for the BLG systems.

# Bibliography

- [1] S. J. Hong, “Electrical properties of modified graphene via doping and stacking”, PhD thesis (Seoul National Univiversity, Dec. 2015).
- [2] P. Blake, E. W. Hill, A. H. Castro Neto, K. S. Novoselov, D. Jiang, R. Yang, T. J. Booth, and A. K. Geim, *Applied Physics Letters* **91**, 063124 (2007).
- [3] K. Kim, S. Coh, L. Z. Tan, W. Regan, J. M. Yuk, E. Chatterjee, M. F. Crommie, M. L. Cohen, S. G. Louie, and A. Zettl, *Physical Review Letters* **108** (2012).
- [4] R. W. Havener, H. Zhuang, L. Brown, R. G. Hennig, and J. Park, *Nano Letters* **12**, 3162–3167 (2012).
- [5] V. Carozo, C. M. Almeida, E. H. M. Ferreira, L. G. Cançado, C. A. Achete, and A. Jorio, *Nano Letters* **11**, 4527–4534 (2011).
- [6] C.-H. Yeh, Y.-C. Lin, Y.-C. Chen, C.-C. Lu, Z. Liu, K. Suenaga, and P.-W. Chiu, *ACS Nano* **8**, 6962–6969 (2014).
- [7] S. J. Hong, H. Kang, M. Park, M. Lee, D. Soler-Delgado, D. H. Jeong, Y. W. Park, and B. H. Kim, *RSC Adv.* **5**, 103276–103279 (2015).
- [8] A. Das, B. Chakraborty, S. Piscanec, S. Pisana, A. K. Sood, and A. C. Ferrari, *Physical Review B* **79** (2009).
- [9] O. Frank, G. Tsoukleri, J. Parthenios, K. Papagelis, I. Riaz, R. Jalil, K. S. Novoselov, and C. Galiotis, *ACS Nano* **4**, 3131–3138 (2010).

- [10] B. H. Kim, S. J. Hong, S. J. Baek, H. Y. Jeong, N. Park, M. Lee, S. W. Lee, M. Park, S. W. Chu, H. S. Shin, J. Lim, J. C. Lee, Y. Jun, and Y. W. Park, *Scientific Reports* **2** (2012).
- [11] S. J. Hong, M. Park, H. Kang, M. Lee, D. Soler-Delgado, D. S. Shin, K. H. Kim, S. Kubatkin, D. H. Jeong, Y. W. Park, et al., *Applied Physics Letters* **106**, 142110 (2015).
- [12] Y. M. Zuev, W. Chang, and P. Kim, *Physical Review Letters* **102** (2009).
- [13] S.-G. Nam, D.-K. Ki, and H.-J. Lee, *Physical Review B* **82** (2010).
- [14] I. Silvestre, E. A. de Morais, A. O. Melo, L. C. Campos, A.-M. B. Goncalves, A. R. Cadore, A. S. Ferlauto, H. Chacham, M. S. C. Mazzoni, and R. G. Lacerda, *ACS Nano* **7**, 6597–6604 (2013).
- [15] K. S. Novoselov, A. K. Geim, S. V. Morozov, D. Jiang, M. I. Katsnelson, I. V. Grigorieva, S. V. Dubonos, and A. A. Firsov, *Nature* **438**, 197–200 (2005).
- [16] J. Katoch, J.-H. Chen, R. Tsuchikawa, C. W. Smith, E. R. Mucciolo, and M. Ishigami, *Physical Review B* **82** (2010).

# Chapter 5

## Summary and Conclusion

In summary, hexagonal twisted bilayer graphene was synthesized by Atmospheric Pressure Chemical Vapor Deposition and transferred to  $\text{SiO}_2$  substrates. Optical microscopy and Raman spectroscopy were used to estimate the twist angle  $\theta$  on the tBLG flakes. After the angle identification, the tBLG flakes were etched and four devices with different stacking angles, ranging from small to large twist, were fabricated. The devices were build either on field-effect transistor or thermoelectric power configuration. Finally, the four devices were subjected to 11 bar of pure hydrogen at 350 K inside of a high-pressure/high-vacuum chamber, where all the measurements were performed.

As a result of hydrogenation, it was found that all the devices, regardless of  $\theta$ , showed a N-type doping behaviour upon hydrogen exposure. This effect was notorious on the transfer curves as the  $V_{\text{CNP}}$  shifts towards negative values as the exposure time increases. By measuring the Seebeck coefficient ( $S$ ) as a function of  $V_G$  on the small angle sample, the negative shift on the zero-crossing point of  $S$  supported the observation of electron doping as seen on the transfer curves, and the unaffected shape of the  $S$  curve indicates the preservation of the electronic structure similar to the SLG case. Furthermore, post-hydrogenation Raman spec-

troscopy studies showed a unbalanced blue-shift on the G and 2D peaks, resulted from the competition between electron doping and lattice compression, suggesting the formation of the C-H bond due to dissociation of the H<sub>2</sub> molecule on the CVD-grown tBLG surface, in agreement with previous studies.

Finally, in spite of exploring the evolution of the hydrogenation process, the change of the V<sub>CNP</sub> and the carrier mobilities were extracted from the transfer curves and studied as a function of time. For the case of the V<sub>CNP</sub>, since  $|\Delta V_{CNP}| \propto n_{imp}$ , the exponential trend of our curves follows a first-order adsorption model of the hydrogen atoms on graphene, by which it is possible to estimate of the rate of the C-H bond formation and the available carbon sites due to the limited nature of the process. Moreover, this behaviour has been previously observed in exfoliated BLG samples and appears to be an intrinsic feature of bilayer graphene systems. Similarly, the evolution of the carrier mobilities of the tBLG flakes showed an exponentially asymmetric behaviour for electrons and holes, increasing for former and decreasing for latter. This characteristic evolution is better understood by taking account the substrate effects, which hinders the decreasing effect in both mobilities of hydrogen adsorbates as they been classified as short-range scatterers

Therefore, while the present work helps in understanding the hydrogenation process on bilayer graphene with different stacking configurations, there is a need to extend the hydrogenation studies of CVD-grown tBLG over high-quality substrates to have a clearer picture on the evolution of the hydrogen interaction with tBLG and understand the its role on the carrier transport in graphene.

## 국문 초록

그래핀의 수소흡착은 전자 도핑과 같은 수송 특성의 변화로 인해 주목을 끈다. 박리형 그래핀의 수소결합에 대한 연구는 현재까지 이루어졌으나 틀어진 이중층 그래핀과 같이 더 높은 자유도가 주어진 이중층 그래핀 시스템의 경우에 대한 특성 연구는 많이 이루어지지 않고 있다. 이 논문에서 우리는 화학기상증착법(CVD)으로 키운, 이중층 그래핀 소자를 고기압의 수소 환경에 노출시켰다. 라만 분광법을 비롯해 전기 전도도 및 제벡 계수 측정법과 같은 전기적 특성 변화를 통해, 층 간 각도에 무관하게 그래핀 표면에서 수소 해리에 의한 흡착 현상에 기인한 n-타입 도핑 현상이 확인되었다. 이 연구 결과를 통해 수소와 결합된 이중층 그래핀 소자의 기능 변화 및 응용성 연구에 도움을 받을 수 있을 것이다.

키워드 : 틀어진 이중층 그래핀, 수소결합, 전자 도핑, 제벡 계수



### 저작자표시-비영리-변경금지 2.0 대한민국

이용자는 아래의 조건을 따르는 경우에 한하여 자유롭게

- 이 저작물을 복제, 배포, 전송, 전시, 공연 및 방송할 수 있습니다.

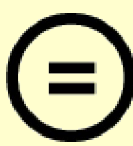
다음과 같은 조건을 따라야 합니다:



저작자표시. 귀하는 원 저작자를 표시하여야 합니다.



비영리. 귀하는 이 저작물을 영리 목적으로 이용할 수 없습니다.



변경금지. 귀하는 이 저작물을 개작, 변형 또는 가공할 수 없습니다.

- 귀하는, 이 저작물의 재이용이나 배포의 경우, 이 저작물에 적용된 이용허락조건을 명확하게 나타내어야 합니다.
- 저작권자로부터 별도의 허가를 받으면 이러한 조건들은 적용되지 않습니다.

저작권법에 따른 이용자의 권리와 책임은 위의 내용에 의하여 영향을 받지 않습니다.

이것은 [이용허락규약\(Legal Code\)](#)을 이해하기 쉽게 요약한 것입니다.

[Disclaimer](#)



Master's Thesis of Science

# N-type doping of bilayer graphene devices by hydrogen adsorption

수소 흡착을 통한 이중층 그래핀 소자의 N-타입  
도핑

February 2016

Graduate School of Physics  
Seoul National University  
Physics Major

David Soler Delgado

# N-type doping of bilayer graphene devices by hydrogen adsorption

**Professor Yung Woo Park**

Submitting a master's thesis of Physics

December 2015

Graduate School of Physics  
Seoul National University  
Physics Major

David Soler Delgado

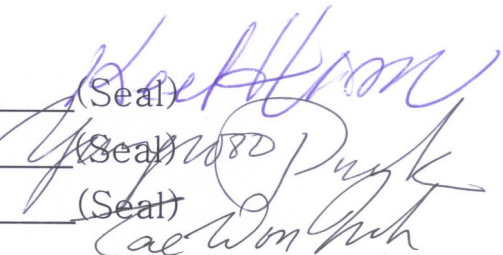
Confirming the master's thesis written by

David Soler Delgado

December 2015

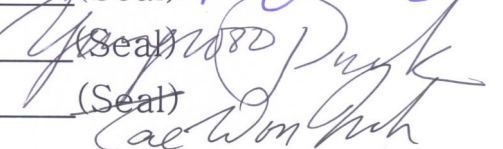
Chair Kee Hoon Kim

(Seal)



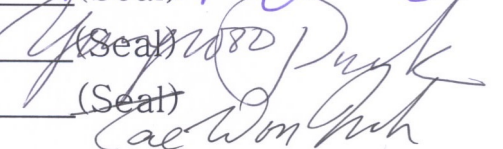
Vice Chair Yung Woo Park

(Seal)



Examiner Tae Won Noh

(Seal)



# **Abstract**

Hydrogenation of graphene has attracted attention due to the modified transport properties such as electron doping. Despite the fact that there has been studies of hydrogenation of exfoliated graphene, there are studies missing for bilayer graphene systems with higher degrees of complexity such as twisted bilayer graphene (tBLG).

In this thesis, we fabricated CVD-grown tBLG graphene devices and exposed them into high-pressure pure molecular hydrogen environment. By means of Raman spectroscopy and electrical characterization methods such as electrical transfer curve and Seebeck coefficient (TEP) measurements, the n-type doping behaviour is confirmed regardless of the twisting angle between the layers, suggesting the H<sub>2</sub> dissociation on the surface of graphene. Our results can be used as an aid for exploring further functionalities of hydrogenated bilayer graphene devices.

**Keyword:** twisted bilayer graphene, hydrogenation, electron doping, Seebeck coefficient.

**Student number:** 2013-23787

# Contents

<b>Abstract</b>	<b>i</b>
<b>1 Introduction</b>	<b>1</b>
1.1 Motivation . . . . .	1
1.1.1 The incursion of carbon in high-performance electronics . . . . .	1
1.1.2 Outline and purpose of this thesis . . . . .	4
<b>2 Background</b>	<b>8</b>
2.1 Single layer graphene . . . . .	8
2.2 Bilayer and twisted bilayer graphene . . . . .	10
2.3 Doping methods of graphene reviewed . . . . .	13
<b>3 Fabrication and experimental procedures</b>	<b>18</b>
3.1 Device Fabrication . . . . .	19
3.1.1 CVD-Growth of twisted bilayer graphene . . . . .	19
3.1.2 E-beam lithography . . . . .	21
3.1.3 Electrode deposition and graphene etching . . . . .	22

3.2	Characterization Techniques . . . . .	23
3.2.1	Raman Spectroscopy . . . . .	23
3.2.2	Electrical measurements . . . . .	25
3.3	Hydrogenation of Graphene devices . . . . .	29
<b>4</b>	<b>N-type doping on CVD-grown twisted bilayer graphene devices by hydrogen adsorption</b>	<b>34</b>
4.1	Identification of CVD-grown twisted bilayer graphene . .	34
4.2	Transfer curves of graphene devices under hydrogen exposure	38
4.3	Raman spectroscopy of hydrogenated tBLG . . . . .	40
4.4	TEP measurements of graphene device under hydrogen exposure . . . . .	42
4.5	Development of device features as hydrogen exposure . .	44
<b>5</b>	<b>Summary and Conclusion</b>	<b>49</b>

# List of Figures

1.1	Low dimensional allotropes of carbon. . . . .	2
1.2	Facts on graphene history. . . . .	3
2.1	Real and reciprocal lattices, and electronic dispersion relation for single layer graphene . . . . .	9
2.2	Real and reciprocal lattices, electronic dispersion and band gap opening for Bernal bilayer graphene . . . . .	10
2.3	Real and reciprocal lattices, electronic dispersion and van Hove singularities for twisted bilayer graphene . . . . .	12
2.4	Examples of graphene doping . . . . .	14
3.1	CVD-growth process and transfer . . . . .	19
3.2	3-step process fabrication of the graphene devices . . . .	21
3.3	Raman spectroscopy scattering processes and graphene spectrum . . . . .	23
3.4	Graphene field-effect transistor schematic and its transfer curve . . . . .	26

3.5	Thermo-electric power measurements schematic, principles and calibration . . . . .	28
3.6	Probe for cryostat and high H <sub>2</sub> pressure . . . . .	30
4.1	Measurement of twist angle of tBLG flakes . . . . .	35
4.2	Raman spectroscopy of tBLG devices with different stacking angles . . . . .	36
4.3	Transfer curves of all our devices as a function of time . .	39
4.4	Raman spectroscopy on the small angle sample before and after hydrogen exposure . . . . .	41
4.5	Seebach coefficient for the critical angle sample before and after hydrogen exposure . . . . .	43
4.6	V <sub>CNP</sub> for different twisted angle as a function of time . .	44
4.7	Evolution of carrier mobility as a H <sub>2</sub> time exposure . . .	45

# List of Tables

4.1	Fitted values of G and 2D peaks for small angle samples	37
4.2	Fitted values of G and 2D peaks, before and after hydrogen exposure . . . . .	40

# Chapter 1

## Introduction

### 1.1 Motivation

#### 1.1.1 The incursion of carbon in high-performance electronics

Since the early beginnings of high-performance electronics, the field effect transistor (FET) has been used as a main building block of our processing cores. As the time goes by, the Moore's law is pushing the limit on the dimensions of these devices up to the point that in some years, silicon, the commercially preferred material for micro/nano electronics, will be no longer usable [2]. In this approach, the nanotechnology and the condensed matter physics fields have a difficult task to find a suitable way of keep the computing power increasing as the device size does the opposite. Several ways have been attempted to overcome this issue, ranging from changing the processing paradigm by encoding information on different degrees of freedom of atoms and electrons, up to looking into novel transistor configuration, including the incorporation of new emergent materials.

Focusing on this last attempt, low-dimensional carbon allotropes have

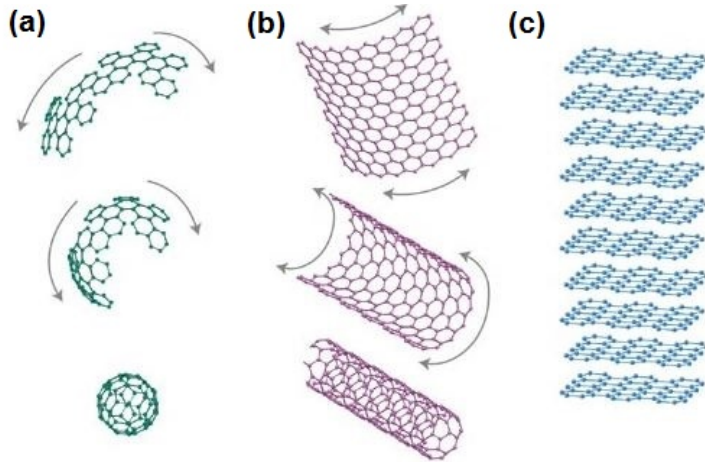


Figure 1.1: Low dimensional allotropes of carbon. (a) Fullerenes, caged configurations of carbon atoms grouped in a spherical shapes (b) Carbon nanotubes, (c) Stacks of single layer graphene. Adapted from [1]

been always considered as a strong candidate, reflected on the amount of research done on this field from its early beginnings. Starting from the zeroth dimensional material of the family, the fullerene [3] (Figure 1.1a), has been tried to be introduced in modern high-performance technologies as n-type channel on field effect transistors, by taking advantage of its solution processability [4]. However its performance is still inferior to the silicon-based well known technologies. Also, due to the interesting physics observed on the fullerene, there have been theoretical approaches exploring the spin degree of freedom of the molecule, in order to be used as a quantum-computer building block but unfortunately, its implementation seems far from now, quenching the chances of incursion of the fullerenes into the field of high-performance electronics in the near future. [5].

Following the discovery timeline, the one-dimensional material of the carbon family, the nanotubes (CNT's), was a bit more promising on its attempt to reach the commercial electronics field, due to their remarkable features such as an high carrier mobility of  $\sim 79,000 \text{ cm}^{-2}/\text{Vs}$  [6] and

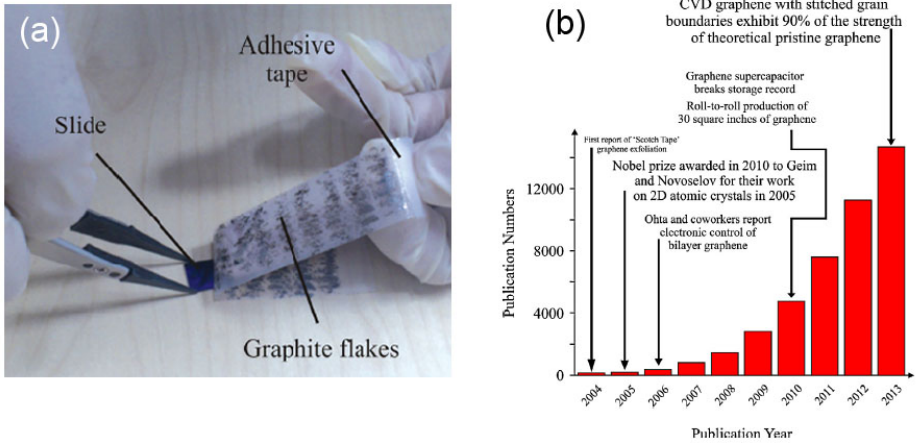


Figure 1.2: (a) Mechanical scotch tape method (b) Publication numbers of graphene after its discovery. Adapted from [8]

the important phenomena observed such as superconductivity and single ballistic transport [7]. Unfortunately, despite the fact of its superior properties of the CNT's, they has not reached the consumer high-performance electronics field either, tentatively suggested by the moderate difficulty on the device processing and manufacturing.

Lastly, graphene (Figure 1.1c), the two-dimensional member of the carbon family and the first two-dimensional material ever isolated, was discovered by Andre Geim and Kostya Novoselov in 2004. Its unique features such as the extremely high mobility ( $\sim 200,000 \text{ cm}^{-1}/\text{Vs}$ ) [9], the ease on device fabrication and the new emergent physics inside it, are not only making it one of the strongest silicon competitors, but also it is leading a revolution in the condensed matter research field as shown in the number of publications after graphene discovery (Figure 1.2b)[8].

However, despite the magnificent graphene characteristics, there are two crucial factors that might impede to reach this goal. The first of them is the production of large scale, high-quality graphene. Although it has

been possible to growth up to 30 inches of continuous sheet by chemical vapor deposition (CVD) methods [10], its carrier mobility is still inferior to the exfoliated graphene flakes obtained from highly oriented graphite (HOPG). The second issue is caused by the intrinsic nature of graphene which is a zero-gap semiconductor with the Fermi level located in the so called Dirac point. It is desirable for high-performance electronics to use gapped semiconductors with the chance of controlling the Fermi level, in order to create complementary electronic structures. Graphene has an extraordinary sensitivity to external environments, where simple interactions such as metal deposition [11], moisture [12] or even exposure to different type of gases and chemicals can induce doping and band-gap opening [13], [14]. Therefore, by finding suitable and robust treatments, it will be possible to tailor the graphene properties, making them fit into the requirements to substitute silicon on the high-performance electronics area.

### 1.1.2 Outline and purpose of this thesis

In this thesis work, we contribute in finding some solution to the second of the problems previously addressed by studying the modification of bilayer graphene upon its exposure into 99.9999%  $H_2$  high-pressure environments. Despite the fact there has been some previous studies about this type of hydrogen interaction with exfoliated single and bilayer graphene [15], there is still a lack of research on the area of CVD-grown bilayer graphenes. Moreover, we exploit the advantages of the CVD method by growing hexagonal bilayer graphene flakes with a rotational mismatch between the layers, also know as twisted bilayer graphene (tBLG). Therefore, by adding this extra degree of complexity, it will be possible to extend our observations for those unexplored bilayer graphene systems, in order to give a broader options on the seek for a suitable graphene modification technique.

For this matter, the present manuscript is structured in the following manner: The following section, Chapter 2, will cover the background subjects whose enforce our motivation and give the necessary insights for the interpretation our data. In chapter 3, the methodology followed on the device fabrication, as well as experimental procedure will be described and justified in detail, whereas Chapter 4, considered as the central piece of this thesis, shows and discusses the major results that this work contributes to the graphene research field. Finally, Chapter 5 summarizes our experiments and findings, and addresses the possible pathways to follow for the future research.

# Bibliography

- [1] A. K. Geim and K. S. Novoselov, *Nature Materials*, 183–191 (2007).
- [2] D. Bishop, *Bell Labs Technical Journal* **10**, 23–28 (2005).
- [3] H. K. Kroto, J. R. Heath, S. C. O. Brien, R. L. Curl, and R. E. Smalley, *Nature* **318**, 162–163 (1985).
- [4] P. H. Wobkenberg, D. D. Bradley, D. Kronholm, J. C. Hummelen, D. M. de Leeuw, M. Cölle, and T. D. Anthopoulos, *Synthetic Metals* **158**, 468–472 (2008).
- [5] J. P. Connerade and V. K. Dolmatov, *Journal of Physics B: Atomic, Molecular and Optical Physics* **48**, 015007 (2015).
- [6] T. Durkop, S. A. Getty, E. Cobas, and M. S. Fuhrer, *Nano Letters* **4**, 35–39 (2004).
- [7] M. Terrones, *Annual Review of Materials Research* **33**, 419–501 (2003).
- [8] E. P. Randviir, D. A. Brownson, and C. E. Banks, *Materials Today* **17**, 426–432 (2014).
- [9] K. S. Novoselov, A. K. Geim, S. V. Morozov, D. Jiang, M. I. Katsnelson, I. V. Grigorieva, S. V. Dubonos, and A. A. Firsov, *Nature* **438**, 197–200 (2005).

- [10] S. Bae, H. Kim, Y. Lee, X. Xu, J.-S. Park, Y. Zheng, J. Balakrishnan, T. Lei, H. Ri Kim, Y. I. Song, Y.-J. Kim, K. S. Kim, B. Özyilmaz, J.-H. Ahn, B. H. Hong, and S. Iijima, *Nature Nanotechnology* **5**, 574–578 (2010).
- [11] Y. Nam, N. Lindvall, J. Sun, Y. W. Park, and A. Yurgens, *Carbon* **50**, 1987–1992 (2012).
- [12] H. Wang, Y. Wu, C. Cong, J. Shang, and T. Yu, *ACS Nano* **4**, 7221–7228 (2010).
- [13] Z. Chen, P. Darancet, L. Wang, A. C. Crowther, Y. Gao, C. R. Dean, T. Taniguchi, K. Watanabe, J. Hone, C. A. Marianetti, and L. E. Brus, *ACS Nano* **8**, 2943–2950 (2014).
- [14] A. J. Samuels and J. D. Carey, *ACS Nano* **7**, 2790–2799 (2013).
- [15] B. H. Kim, S. J. Hong, S. J. Baek, H. Y. Jeong, N. Park, M. Lee, S. W. Lee, M. Park, S. W. Chu, H. S. Shin, J. Lim, J. C. Lee, Y. Jun, and Y. W. Park, *Scientific Reports* **2** (2012).

# Chapter 2

## Background

### 2.1 Single layer graphene

Single layer graphene (SLG) is a one-atom thick, two-dimensional sheet of carbon atoms bonded to their in-plane neighbours due to the  $sp^2$  hybridized atomic orbitals, leading to the creation of one  $\pi$ -bond and three covalent  $\sigma$ -bonds and forming a triangular planar structure with an interatomic distance of 1.42 Å. This atomic structure give rise to the graphene honeycomb lattice that is best represented by a triangular bravais lattice with basis of two atoms per unit cell (A and B), as depicted on Figure 2.1a). The following primitive ( $a$ ) and basis vectors ( $\delta$ ) constitute the crystallographic description of graphene. [1]

$$a_1 = \frac{a}{2}(3, \sqrt{3}) \quad a_2 = \frac{a}{2}(3, -\sqrt{3}) \quad (2.1)$$

$$\delta_1 = (0, 0) \quad \delta_2 = -a(1, 0) \quad (2.2)$$

Thus, the hexagonal graphene structure facilitated the electronic band structure calculation by using the simplest approximation methods, such as the tight-binding method, with a high degree of accuracy on the low-energy region, where valence and conductance bands have a electronic

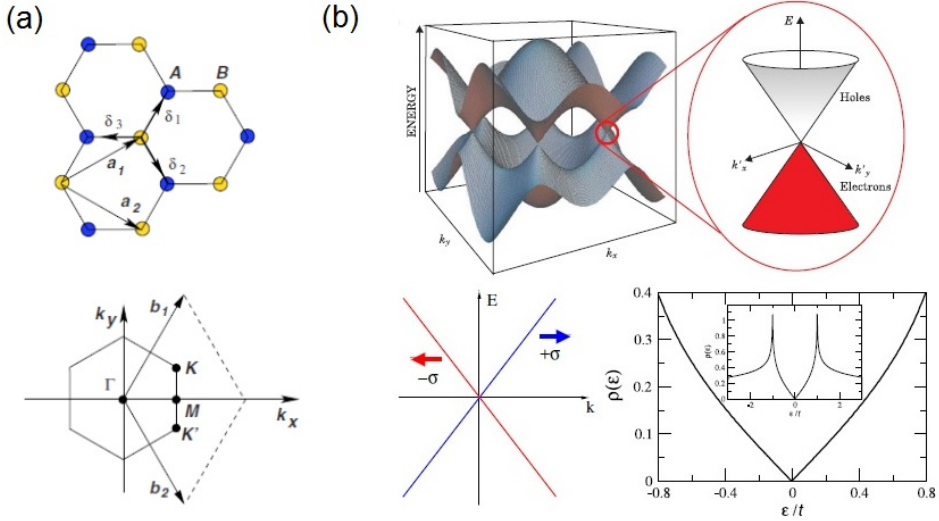


Figure 2.1: (a) Real and reciprocal lattices [1] (b) Electronic dispersion relation with close-up on the K and K' points [2].

linear dispersion relation and touch each other at a single point, the so called Dirac or charge neutrality point, on the K and K' areas of the Brillouin zone (Figure 2.1b).

$$\mathbf{H} = \hbar v_f \begin{pmatrix} 0 & q_x - iq_y \\ q_x + iq_y & 0 \end{pmatrix} = \hbar v_f \sigma \cdot \mathbf{q} \quad (2.3)$$

$$E_{\pm}(q) = \pm \hbar v_f q \quad (2.4)$$

These high symmetry points on the reciprocal space, defines most of the interesting physics of graphene. One of them is the resemblance of the electron transport to that of the massless fermions seen on the (2 + 1) Quantum Electrodynamics, with the difference that the massless Dirac fermions observed in graphene has a reduced velocity of  $v_f \sim 10^6$ , 300 times smaller than the speed of light [1]. Moreover, the identification of this particles has been proved experimentally by the observation of the anomalous quantum hall effect, which is a distinctive signature of

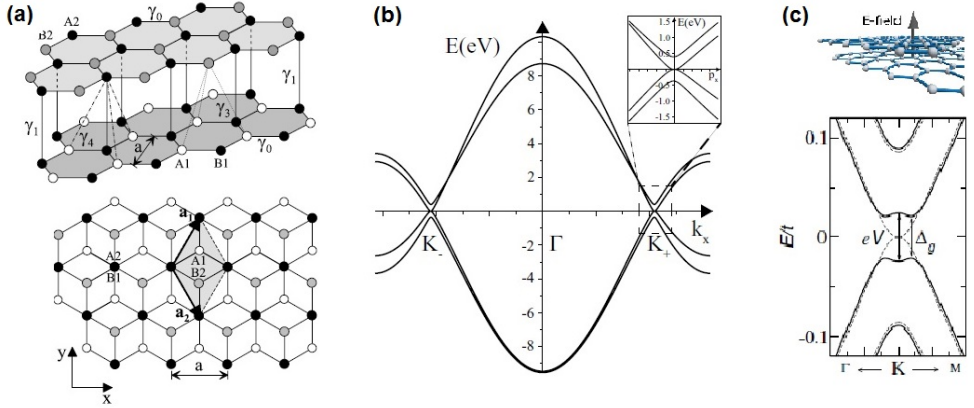


Figure 2.2: (a) Real and reciprocal lattices, (b) Electronic dispersion relation with close-up on the  $K$  and  $K'$  points [5] and (c) Band gap opening under perpendicular displacement field for AB-BLG [6]

Dirac fermions [3]. In addition to the linear dispersion relation, the joint of the bands at the Dirac point turns natural graphene into a semi-metal or a zero-gap semiconductor material with the Fermi level located in the center of the juncture, due to the electron left by the p-orbital making the bands half-filled. [4].

## 2.2 Bilayer and twisted bilayer graphene

One of the main factors that lead to the graphene discovery was the ease of isolating single layer graphene flakes by the "scotch tape method" due to the fact that graphene layers are bonded by dispersive van der Waals forces, which are hundreds of magnitude smaller to the intra-layer binding forces. Therefore, multilayer graphenes, whose appear as an intermediate systems between SLG and bulk graphite, are attractive since the coupling of stacked graphene layers makes the SLG properties to differ as the number of them changes. In this insight, bilayer graphene (BLG) has been one of the most explored graphenes, due to the close resemblance of the electronic transport to SLG, in addition to the new phenomena

observed in some of such types of systems. Moreover, apart from the number of layers, BLG can be sub-classified depending on its stacking order, where Bernal stacked bilayer graphene (or AB-BLG) and twisted bilayer graphene (tBLG) are two of the most explored BLG variants.

Bernal stacked graphene is called to the bilayer graphene where the layers are arranged so that one of the atoms from the lower layer (called B1) is directly below an atom (A2), from the upper layer. (Figure 2.2a). This atomic configuration can be also simply described by a simple crystal structure where the unit cell contains four atoms, labelled as A1, B1 and A2, B2 for the first and second layer respectively. Moreover, due to the weakly intra-layer coupling, the linear dispersion relation for conductance and valence bands of SLG transforms into a parabolic one, but leaving the zero-gap behaviour which gives rise to the massive Dirac fermions travelling at a reduced effective velocity (Figure 2.2b) [5]. Also, in contrast to natural SLG, the application of displacement field perpendicular to the BLG surface induces an asymmetry in the on-site electron energies of the top and bottom layers, leading to a band gap opening on the charge neutrality points at the K and K' areas, an interesting feature to be promising for electronic applications (Figure 2.2)[6].

On the other hand, on twisted bilayer graphene (tBLG), there exists a rotational mismatch  $\theta$  between the layers as depicted on Figure 2.3a. Consequently, the reciprocal space changes accordingly and it is necessary to redefine the basis vectors (only for commensurate cases) for each  $\theta$  angle, making impossible to unambiguously determine a single electronic spectrum for tBLG systems. However, it is possible to identify some trends on the electronic behaviour as a function of the twisting angle. For these purposes, the unit cell of tBLG can be represented as two decoupled SLG unit cells twisted by the same  $\theta$  angle where their corners, the Dirac cones at K and K', are separated by a distance  $\Delta K$ .

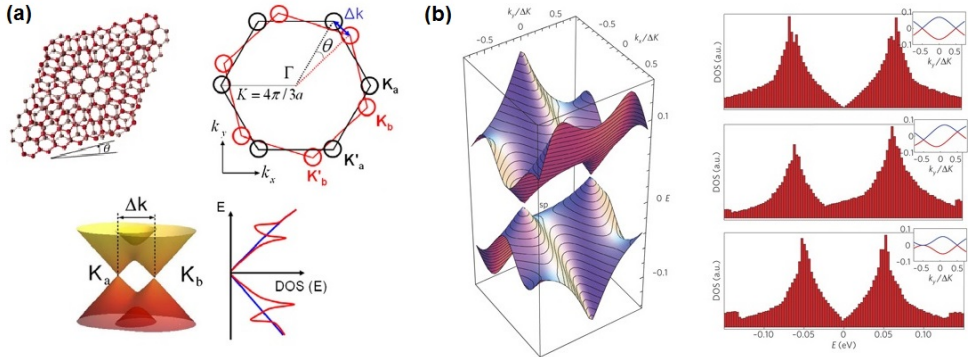


Figure 2.3: (a) Real and reciprocal lattices, electronic dispersion [7] and (b) van Hove singularities for twisted bilayer graphene [8]

proportional to the twist angle [9].

For the case of low-twist angles,  $\theta \approx 0^\circ$ ,  $\Delta K$  decreases and the Dirac cones of the layers overlaps, giving as a consequence an electronic structure resembling to that of AB-BLG. As  $\theta$  increases,  $\Delta K$  increases as well and the Dirac cones start to split until they are totally decoupled at  $\theta \approx 30^\circ$ . At this point the electronic transport is expected to behave similarly to that of two independent single graphene layers (Figure 2.3b) [10]. The behaviours of electronic transport for angles  $\theta > 30^\circ$  can be translated in the sub-thirty region cases due to the rotational symmetry of the structure, whereas detailed explanation of the electronic behaviour on intermediate angles,  $0 < \theta < 30^\circ$  is complicated due to the appearance of additional factors that might make deviate the electronic behaviour from an smooth transition between a AB-BLG system to a double SLG system [7]. However, these additional factors changes the opto-electronic properties of the material due to the appearance of new phenomena, such as the van Hove singularities (vHs) on the low energy region of the electronic spectrum (Figure 2.3b) [8], making possible the identification of the twist angle. Therefore, tBLG can still serve as an important tool for study different BLG systems as this extra degree of complexity, the

$\theta$  angle, can tune the intra-layer coupling in an suitable and controlled manner.

Finally, the particular graphene physical and electronic structure have hundreds of applications not only on the high-performance electronics field where, its extremely high mobility have been used for the production of terahertz transistors [11], but also graphene has been used in some other approaches such as: black-body light emitters due to excellent thermal conductivity [12], resistance standard due to the ease of accessibility to the fundamental constants through the quantum hall effect [13], transparent electrodes due to its low light absorption on the visible range [14] and chemical sensing due to extreme sensitivity of graphene to different environments [15], just to mention some of them.

## 2.3 Doping methods of graphene reviewed

Despite the remarkable properties of natural graphene samples, there exists a need of tailoring graphene properties in order to make them fit into some specific purposes. For this matter, doping processes have been extensively used to tune the electronic transport on graphene, since rather than simply control the Fermi energy level ( $E_F$ ), it has been possible to induce band-gap opening [18] and enhance spin-orbit coupling [19] by different means, which some of them will be discussed next.

In general, graphene doping techniques exploit the low dimensional nature of this material, where surface and interface physics play an important role in the doping process since, by simply changing the surrounding environment, it is possible to tune the electron and hole concentration. In this insight, graphene doping has been simply achieved upon exposure to different type of molecular gases, including  $O_2$  and  $H_2$ . For the first of

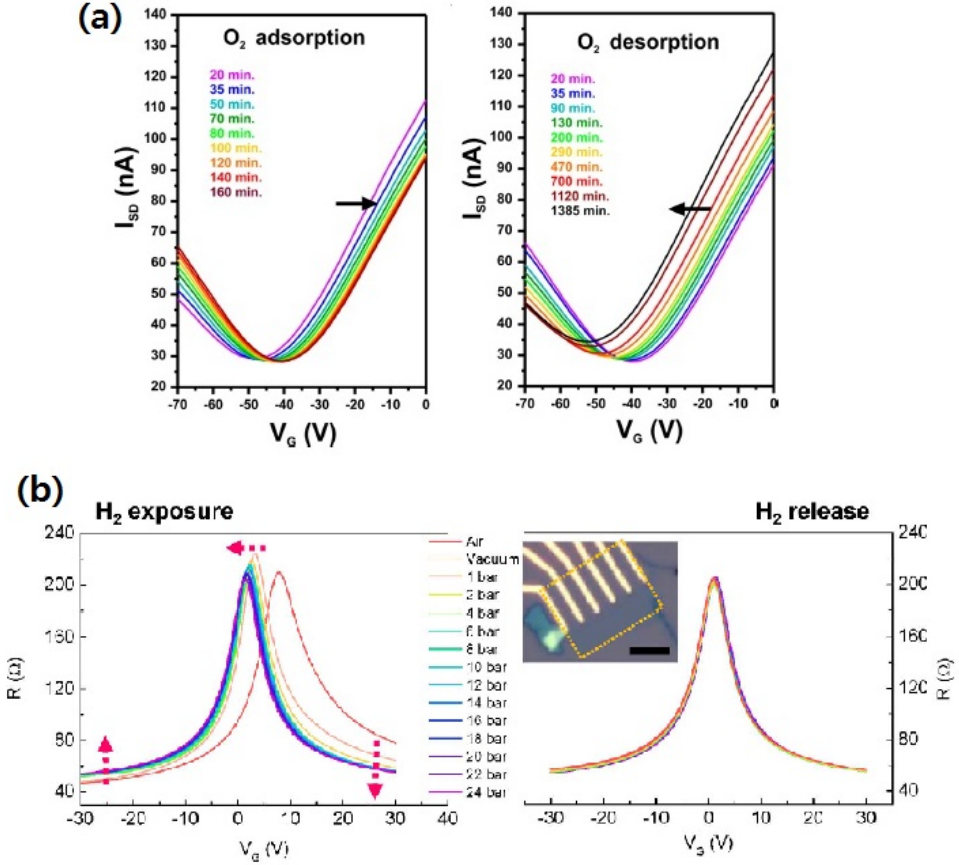


Figure 2.4: Doping of graphene samples before and after (a) O<sub>2</sub> [16] and (b) H<sub>2</sub> [17] exposure.

In the cases, it has been reported that O<sub>2</sub> produces gradual hole-doping as time develops due to the physisorption of the molecules on the graphene sample [16]. The physisorption process is explained as a small perturbation on the electronic structure of the molecules and the sample due to the interaction among them, without the formation of any chemical bonds or changes on the chemical structure. As a consequence, the doping induced by O<sub>2</sub> disappears after the normal atmospheric conditions are restored (Figure 2.4a)

On the other hand, hydrogen/graphene interactions, the ones that

this work is focused on, are reported to be governed by chemisorption, described by stronger perturbations that lead to the hybridization of orbitals and formation of covalent bonds. By exposing exfoliated graphene samples to ultra pure, high temperature, high-pressure H<sub>2</sub> atmospheres, the H<sub>2</sub> molecules dissociates at the surface of the graphene leading to the formation of C-H bonds. While one of the two H<sub>2</sub> electrons participates on the covalent bonding, the remaining electron becomes delocalized on the graphene sample, increasing the electron concentration and a consequent n-type doping effect is observed [20]. Moreover, once the process is stopped and normal conditions are restored, the sample retains its hydrogenated properties, which are observed to only disappear by thermal treatments (Figure 2.4b), reinforcing the claims about the chemisorption nature of the doping process. Therefore, due to its relative stability, graphene electron doping by means of hydrogen dissociation can be used to explore new approaches for graphene functionalization towards the incursion of this material into modern electronics.

# Bibliography

- [1] A. H. Castro Neto, F. Guinea, N. M. R. Peres, K. S. Novoselov, and A. K. Geim, *Reviews of Modern Physics* **81**, 109–162 (2009).
- [2] S. Das Sarma, S. Adam, E. H. Hwang, and E. Rossi, *Reviews of Modern Physics* **83**, 407–470 (2011).
- [3] Y. Zhang, Y.-W. Tan, H. L. Stormer, and P. Kim, *Nature* **438**, 201–204 (2005).
- [4] K. S. Novoselov, A. K. Geim, S. V. Morozov, D. Jiang, M. I. Katsnelson, I. V. Grigorieva, S. V. Dubonos, and A. A. Firsov, *Nature* **438**, 197–200 (2005).
- [5] E. McCann and M. Koshino, *Reports on Progress in Physics* **76**, 056503 (2013).
- [6] E. V. Castro, K. S. Novoselov, S. V. Morozov, N. M. R. Peres, J. M. B. L. dos Santos, J. Nilsson, F. Guinea, A. K. Geim, and A. H. C. Neto, *Physical Review Letters* **99** (2007).
- [7] K. Kim, S. Coh, L. Z. Tan, W. Regan, J. M. Yuk, E. Chatterjee, M. F. Crommie, M. L. Cohen, S. G. Louie, and A. Zettl, *Physical Review Letters* **108** (2012).
- [8] G. Li, A. Luican, J. M. B. Lopes dos Santos, A. H. Castro Neto, A. Reina, J. Kong, and E. Y. Andrei, *Nature Physics* **6**, 109–113 (2009).
- [9] A. O. Sboychakov, A. L. Rakhmanov, A. V. Rozhkov, and F. Nori, *Physical Review B* **92** (2015).

- [10] L.-J. Yin, J.-B. Qiao, W.-X. Wang, W.-J. Zuo, W. Yan, R. Xu, R.-F. Dou, J.-C. Nie, and L. He, *Physical Review B* **92** (2015).
- [11] J. Zheng, L. Wang, R. Quhe, Q. Liu, H. Li, D. Yu, W.-N. Mei, J. Shi, Z. Gao, and J. Lu, *Scientific Reports* **3** (2013).
- [12] Y. D. Kim, H. Kim, Y. Cho, J. H. Ryoo, C.-H. Park, P. Kim, Y. S. Kim, S. Lee, Y. Li, S.-N. Park, Y. Shim Yoo, D. Yoon, V. E. Dorgan, E. Pop, T. F. Heinz, J. Hone, S.-H. Chun, H. Cheong, S. W. Lee, M.-H. Bae, and Y. D. Park, *Nature Nanotechnology* **10**, 676–681 (2015).
- [13] T. Yager, A. Lartsev, K. Cedergren, R. Yakimova, V. Panchal, O. Kazakova, A. Tzalenchuk, K. H. Kim, Y. W. Park, S. Lara-Avila, and S. Kubatkin, *AIP Advances* **5**, 087134 (2015).
- [14] K. Rana, J. Singh, and J.-H. Ahn, *Journal of Materials Chemistry C* **2**, 2646 (2014).
- [15] Daniel Rodrigo, Odeta Limaj, Davide Janner, Dordaneh Etezadi, F. Javier García de Abajo, Valerio Pruneri, and Hatice Altug, *Science* **349**, 161–165 (2015).
- [16] I. Silvestre, E. A. de Moraes, A. O. Melo, L. C. Campos, A.-M. B. Goncalves, A. R. Cadore, A. S. Ferlauto, H. Chacham, M. S. C. Mazzoni, and R. G. Lacerda, *ACS Nano* **7**, 6597–6604 (2013).
- [17] B. H. Kim, S. J. Hong, S. J. Baek, H. Y. Jeong, N. Park, M. Lee, S. W. Lee, M. Park, S. W. Chu, H. S. Shin, J. Lim, J. C. Lee, Y. Jun, and Y. W. Park, *Scientific Reports* **2** (2012).
- [18] A. J. Samuels and J. D. Carey, *ACS Nano* **7**, 2790–2799 (2013).
- [19] J. Balakrishnan, G. Kok Wai Koon, M. Jaiswal, A. H. Castro Neto, and B. Özyilmaz, *Nature Physics* **9**, 284–287 (2013).
- [20] S. J. Hong, M. Park, H. Kang, M. Lee, D. Soler-Delgado, D. S. Shin, K. H. Kim, S. Kubatkin, D. H. Jeong, Y. W. Park, et al., *Applied Physics Letters* **106**, 142110 (2015).

# **Chapter 3**

## **Fabrication and experimental procedures**

In this section, all the procedures followed for the fabrication and characterization of the devices will be introduced. In order to study the modifications on the carrier transport properties of graphene upon exposure to hydrogen environments, several graphene devices were build on 3 step-basis: Growth and transfer of CVD-grown graphene into  $\text{SiO}_2$  substrates, graphene etching and electrode deposition. The crucial factors that lead to a correct fabrication of the final devices which will be explained in detail. As characterization tools, our research is based on three primary methods: Raman spectroscopy, Thermo-electric power measurement and gate-dependent I-V measurements. The configurations for these setups and the details needed for the correct execution of the measurements will be discussed as well.

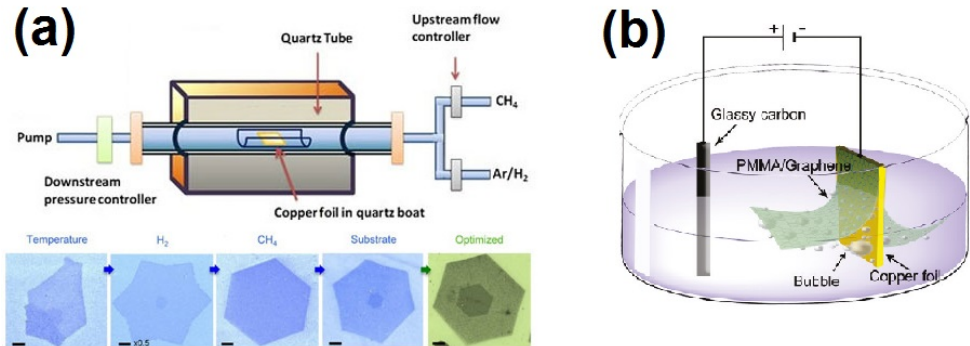


Figure 3.1: (a) CVD-process and optimization of CVD-grown tBLG flakes [5] (b) Electrochemical delamination method for graphene transfer [6]

## 3.1 Device Fabrication

### 3.1.1 CVD-Growth of twisted bilayer graphene

Chemical vapor deposition (CVD) of graphene was first reported in 2008 and 2009 [1], [2] and since then, it has been improved in order to get large areas of high-quality of graphene, where reports indicate coverage areas as large as 30 inches, enough for most of its uses on electronic applications [3]. The CVD method is based on the decomposition of a source gas (usually Methene) into carbon radicals on the top of metal substrates at high temperatures. In addition to serve as a support, metal substrates are used due to its catalytic behavior on the decomposition of the hydrocarbons and determines the graphene growth mechanism, which directly affects its quality [4].

Despite the fact that CVD-grown graphene has shown lower mobilities compared with the exfoliated graphene obtained from Highly Oriented Pyrolytic Graphite (HOPG), the CVD growth method has been extensively used due to the possibility of obtain single and multilayer graphene by modifying the growth conditions. In this manner, we exploit the advantages of the CVD method by using the Atmospheric Pressure

Chemical Vapor deposition (AP-CVD) variant in order to grow hexagonal multilayer crystalites with different stacking angle (tBLG). As it is shown on Figure 3.1a , a fine tuning of the growth conditions is necessary for obtaining spaced uniform multilayer hexagonal crystalites. During our growth process, finding a correct balance on the flow rates of the the source (Ar) and etchant ( $H_2$  ) gases, was crucial for obtaining high-quality tBLG flakes as both of them constitute the self-limiting growth process [7]. Therefore, by following the procedures described in detail elsewhere [8], we synthesized hexagonal twisted bilayer grapehene (tBLG) as follows: High purity copper foil (Alfa aesar 10950, 99.999%) was polished chemically and mechanically in prior to the growth of tBLG. The growth was performed at  $1057^\circ C$  with 500, 30-35, and 2 sccm of Ar,  $H_2$  , and  $CH_4$  (1%, balanced by 99% Ar), respectively, for 15 to 20 min. After growth, the sample cooled rapidly with 1000 and 7 sccm of Ar and  $H_2$  , respectively.

In preparation for the transferring processes, after the growth, PMMA 950k (MicroChem) was spun over one of the sides of the copper foil. The PMMA with the graphene underneath was detached from the foil by electrochemical delamination method of the copper by carefully submerging the PMMA / Graphene / Cu stack onto a 0.1 M NaOH solution in DI wa-ter [6]. Additionally, an external electrostatic potential must to be used to make the reaction favourable. Therefore, one clamp of the voltage source must be connected to some exposed copper parts on the stack, while the other clamp is directly submerged into the solution. A small potential difference at the voltage source (approximately 4 V) will be sufficient to make bubbling appear at the clamps as well as at the edges of the copper stack, indicating the progress of the reaction. As the time goes by, the PMMA film, with the graphene underneath, will be completely detached and floating on the solution where it should be picked up gently in order to keep the graphene side of the film clean. After rinsing the film on

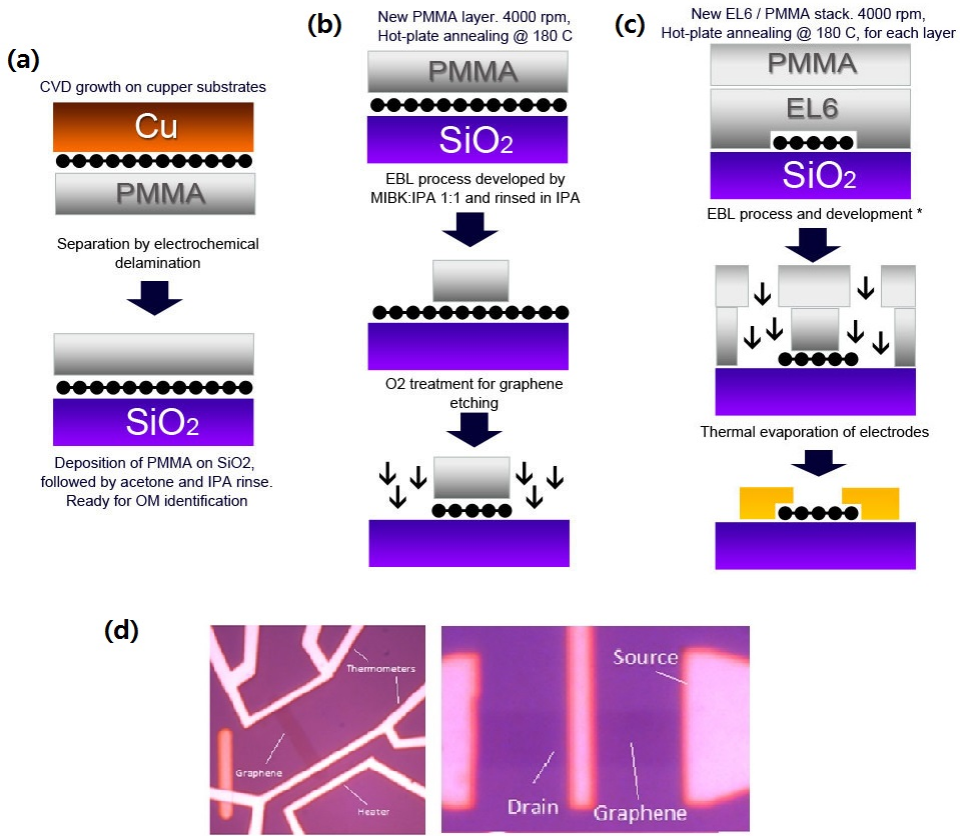


Figure 3.2: 3-step process fabrication of the graphene devices used in this work. (a) Graphene growth, transfer and optical identification, (b) graphene etching, (c) Electrode deposition and (d) Finished devices

DI water, the PMMA is placed on the top of the SiO<sub>2</sub> substrates with their backside was previously etched by BOE, in order use the exposed silicon as gate. Finally, the PMMA laying on the top of graphene can be removed easily by an acetone and IPA rinse (Figure 3.2a).

### 3.1.2 E-beam lithography

For our device preparation, two different EBL procedures were followed depending on the processing stage in course: electrode deposition or

graphene etching. For electrode deposition, a co-polymer / polymer stack consisting of EL6 and PMMA 950k (MicroChem) was spun on the top of graphene. The underneath co-polymer has higher electron-sensitivity than the PMMA, which translates it into a bigger etched area once the lithography is developed (Figure 3.2c), leaving an offset with respect of the PMMA layer. As a consequence, when the electrodes are deposited, the metals do not touch the inner walls of the cavities made on the polymer stack, making the lift-off process easier. For the graphene etching step, instead of a bilayer polymer structure, a single layer of 20 nm PPMA 950k was used. In both types of EBL process, the lithography was performed using a Tescan Mira-3 FE-SEM equipped with a NPGS system for nano-patterning at a 20 kV, with doses  $\sim 200 \mu C/cm^2$ . For developing process, a common solution MIBK:IPA 1:1, was used in which the EBL-exposed substrate was soaked for a few seconds followed by an IPA rinse.

### 3.1.3 Electrode deposition and graphene etching

The electrode deposition process consisted of a EBL process described above followed by a standard thermal evaporation to create a stack of Cr/Au of 3 nm/100 nm, respectively. The Lift-off procedure was done by immersing the samples into a acetone bath for several hours and finally rinsed with IPA. The graphene etching process was performed by O<sub>2</sub> plasma treatment following the procedures described elsewhere [9]. For masking purposes, a single layer EBL process, as described above, was used in order to select suitable rectangular areas on the tBLG flakes. After EBL and etching processes, the remaining PMMA was cleaned by an acetone and IPA rinse. Finally, an overall description of our fabrication process, including some of the details not mentioned on the main text, is shown on Figure 3.2.

## 3.2 Characterization Techniques

### 3.2.1 Raman Spectroscopy

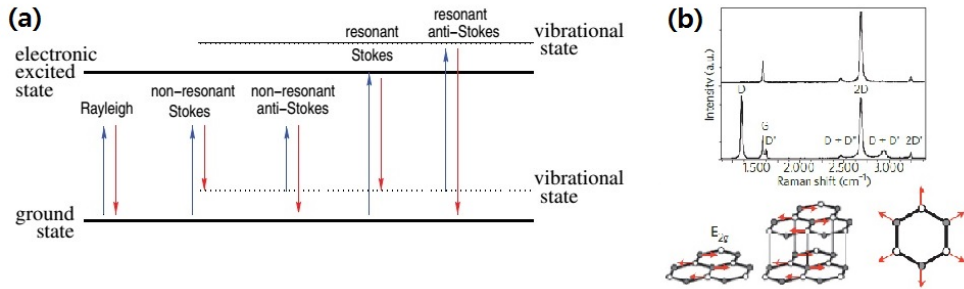


Figure 3.3: (a) Raman spectroscopy scattering processes, and the different types of light scattering. (b) Raman processes on graphene. [10]

Light-matter interactions have been useful for determining the structural and electronic properties of different materials, since as photons interacts with matter, elastic and inelastic scattering processes take place. On elastic scattering, also known as Rayleigh scattering, the energy of the out-coming photon ( $\hbar_{SC}$ ) equals that of the incoming photon ( $\hbar_L$ ). By using the energy states representation of the target to explain the elastic scattering, the photon induces a electron transition into the so-called "virtual states" which decays into the initial stationary level as the electron did not reach any higher energetic level.

In contrast to the Rayleigh scattering, inelastic scattering, also known as Raman scattering, may occur in parallel to Rayleigh scattering but at lower probability. For this process, the energies of the incident and emitted light are different, making necessary to sub-classify the Raman scattering, depending on the initial and final energetic configurations of the sample. Stokes scattering is named to the type of Raman scattering where the incoming photon is absorbed and induces an electronic transition from initial stationary state into a higher-energetic virtual state.

However, instead of returning to the initial state as the elastic case, some electrons may decay into other vibrational states with higher energies than the initial one. Therefore, the energy of the emitted photon will be decreased by an amount  $\hbar\omega_{SC} = \hbar\omega_L - \hbar\omega_\Omega$ , where  $\hbar\omega_\Omega$  is the energy difference between the initial and excited state. On the other hand, Raman Anti-stokes scattering is based on the same transition mechanism, however there exists the probability that before the photon excitation, some electrons are in higher vibrational states. In this case, the photon absorption on these electrons will excite them and make them return into the lower stationary state, emitting a photon with high energy than the incoming one by an amount:  $\hbar\omega_{SC} = \hbar\omega_L - \hbar\omega_\Omega$  as depicted on Figure 3.3a

Raman spectroscopy has its basis on these two light inelastic scattering processes, by measuring the intensity of scattered light as a function of the difference between the incident and scattered photon energy, the so-called "Raman shift" historically plotted in  $cm^{-1}$  units. Therefore, since it is possible to access to the structural and electronic information of the sample, this characterization method has been extensively used for material analysis in an non-destructive way [10].

In the case of graphene, Raman spectroscopy has been useful in determining doping [11], thickness detection [10] and strain [12]. This has been possible due to the high sensibility of graphene to external factors, where the most of the analysis are based on the following peaks of its spectrum: The G-band ( $\sim 1580 cm^{-1}$ ) which is related to the double degenerate zone center  $E_{2g}$  mode. The D-band ( $\sim 1350 cm^{-1}$ ), related as a breathing mode of the  $A_{1g}$  symmetry and which presence is attributed to disordered samples. The 2D-band ( $\sim 2700 cm^{-1}$ ), originated from a second-order process, involving two iTO phonons near the K point [13], and the R-R' peaks which are signature of the existence of twisting angle

between layers [5].

For our research, Raman spectroscopy was used for two main purposes: First, to detect twisted angle on bilayer structures, this characterization was done on all devices. And second, to verify and support our observations on the hydrogenation processes that were mainly characterized by means of electrical measurements. All our Raman characterization measurements were performed using a LabRam 300 by JY-Horiba spectrometer, with a wavelength of 532 nm and a laser power of 0.2 mW in order to avoid any damage of the devices.

### 3.2.2 Electrical measurements

Since the early beginnings of the graphene research, gated electrical measurements have been selected as the preferred characterization method, not only to its relative ease of execution, but also because its attributes give important information about the electronic structure, due to the possibility of tuning the carrier concentration and evidently the Fermi level of the graphene devices. For this reason, we based our electrical characterization in 2 types of gated measurements. Gate-dependent I-V measurements (Also known as transfer curve method) and Thermo-electric power measurements.

#### Gate-dependent I-V measurements

Figure 3.4a shows the schematic of the simplest of our characterization methods and a common transfer curve for a field effect transistor (FET) configuration where pristine graphene acts as a channel. The peculiar form of the pristine graphene transfer curve reveals the linear dispersion nature of the low-energy region, where the Dirac point on the momentum space is translated onto a minimum conductance point (also known as

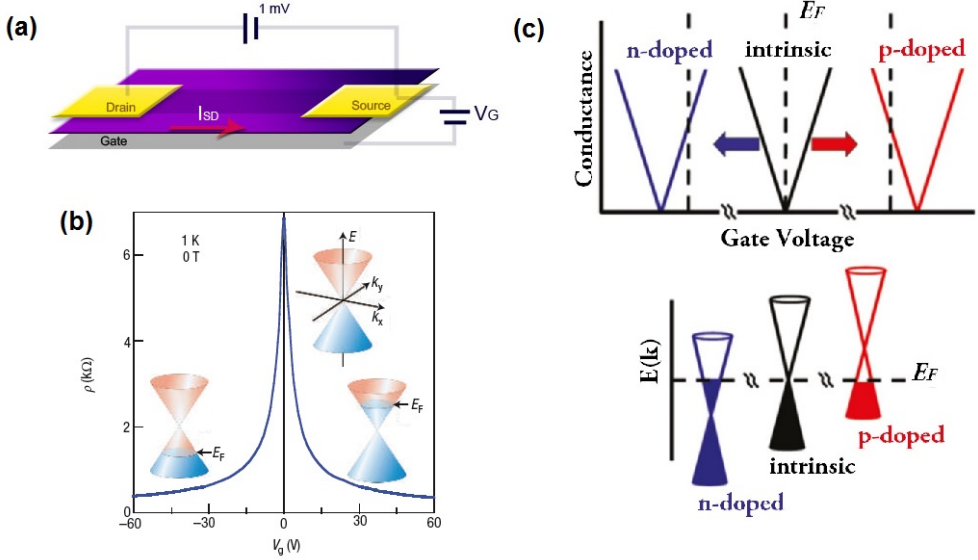


Figure 3.4: (a) Schematic of graphene FET showing the potential bias configuration, (b) Transfer curve of pristine single layer graphene denoted as a graph of  $V_G$ -Resistance or  $V_G$ -Conductance [14]. (c) Electron and hole doping representation on the energy dispersion diagram and the transfer curves

$V_{CNP}$ ) at  $V_G = 0$ . Due to the fact that the potential difference  $V_G$  can be translated into an effective induced carrier density inside the sample by:

$$n_{ind} = \frac{C_G}{e}(V_G - V_{CNP}) \quad (3.1)$$

where  $C_G$ ,  $e$ ,  $V_G$  and  $V_{Dirac}$  are the capacitance per unit area, electron charge, gate voltage and the minimum conductance voltage or CNP, respectively, it is possible to control the population of the low-energy levels of graphene and as a consequence monitor electronic changes on our samples in on this region [14].

One of the most characteristic phenomena observed on the transfer curves is the doping effect. On pristine graphene, the Fermi energy ( $E_F$ ) is placed right on the Dirac point at the 0 eV. However, whenever there

exists additional holes or electrons, the  $E_F$  is shifted upwards towards the conduction band or downwards towards the valance band. In our transfer curves, this is directly reflected by a shift on the  $V_{CNP}$  towards positive values in case of hole doping and towards negative values in case of electron doping, as it can be depicted on Figure 3.4c.

In our measurements, the gate-dependent I-V curves were measured frequently, in order to study the temporal evolution of the hydrogen effects on the CVD-grown hexagonal twisted bilayer graphene devices by using an 4200-SCS Keithley Parameter Analyzer. All the measurements were performed on a two probe, steady-state configuration (DC characterization) with a  $V_{DS} < 1mV$  to avoid damages on our samples.

### **Thermoelectric power measurements**

The Seebeck coefficient ( $S$ ), also know as Thermo-electric power (TEP), represents the relation between the temperature gradient  $\nabla T$  and the electric field  $E$  across the sample in an open-circuit configuration such as  $\vec{E} = S \nabla \vec{T}$ . When a material is subject to heating, the main carriers inside of it respond to the temperature gradient moving from the hot to the cold region. This charge movement produces an electric field, which retards the thermal diffusion until it reaches an equilibrium configuration leading a zero net carrier flow.

Therefore, by measuring the potential drop  $\Delta V$  on the hot and cold regions as depicted on Figure 4.5a, it is possible to specify  $S$ , which is positive ( $S > 0$ ) or negative ( $S < 0$ ) when the main carriers on the sample are holes or electrons, respectively. Moreover, in addition to the potential measurement, the hot and cold electrodes are used to measure the temperature gradient by establishing the relation between the resistance of the electrode as function of the temperature as depicted on Figure 3.5b.

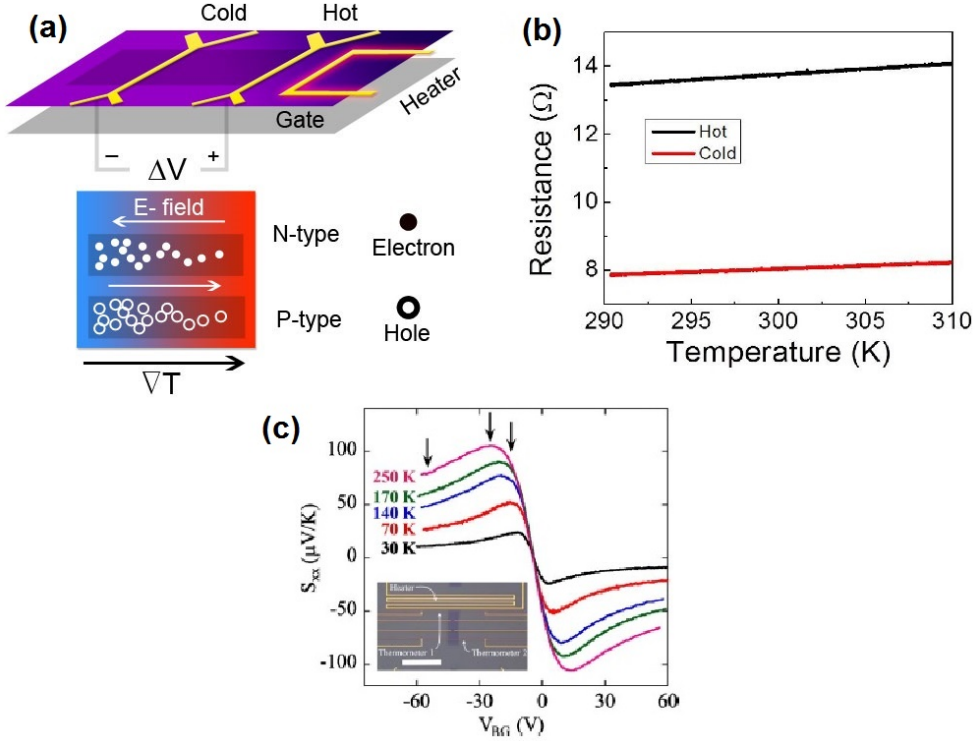


Figure 3.5: (a) Schematic showing principle of operation of thermoelectric power measurement (b) Calibration curve for the set of thermometers and (c) graphene Seebeck coefficient as a function of gate-voltage [15]

For the case of graphene, thermoelectric power, in conjunction with the gating mechanism, has been used to explore the carrier transport inside the material. Figure 4.5c, shows a particular curve of these measurements done on pristine graphene [15]. As it is expected from the transfer curve measurements, the Seebeck coefficient have a transition from positive to negative values, close to the  $V_G = 0$ , indicating the change on the main carrier from holes to electrons. Furthermore, it has been demonstrated that graphene, as well as carbon nanotubes, follow the semi-classical Mott's relation, reinforcing the usefulness of the Boltz-

mann transport formalism [16]:

$$S = -\frac{\pi^2 k_B^2 T}{3|e|} \frac{1}{\sigma} \frac{d\sigma}{dV_G} \frac{dV_G}{dE} \Big|_{E=E_F} \quad (3.2)$$

where  $\sigma$ ,  $k_B$ ,  $T$  and  $V_G$  are the conductivity, Boltzmann constant, temperature and gate voltage, respectively.

In our measurements, the TEP where performed on hydrogenated and pristine graphene conditions in order to support our results obtained by the transfer curve method. In all our experiments, TEP was performed an standard steady-state technique with a temperature gradient such that  $\Delta T \ll T$ .

### 3.3 Hydrogenation of Graphene devices

As a conclusion for the current chapter, a general summary of the fabrication and experimental procedures is presented for further references. Once the growth and transfer procedures of our CVD hexagonal twisted bilayer graphene were performed, the  $\text{SiO}_2$  substrates were inspected by optical microscopy to select suitable crystallites, which its twisted nature was cross verified by Raman spectroscopy measurements prior any hydrogen treatment. Further fabrication processes were executed to the make graphene devices on the field-effect transistor or thermo-electric power configuration.

To study the effects of hydrogen on hexagonal twisted bilayer graphene devices, a high-vacuum / high-pressure chamber, depicted on Figure 3.6, was used, where all the electrical characterization measurements were performed without exposing the sample to atmosphere conditions. Upon the fabrication, the graphene devices were introduced into the chamber

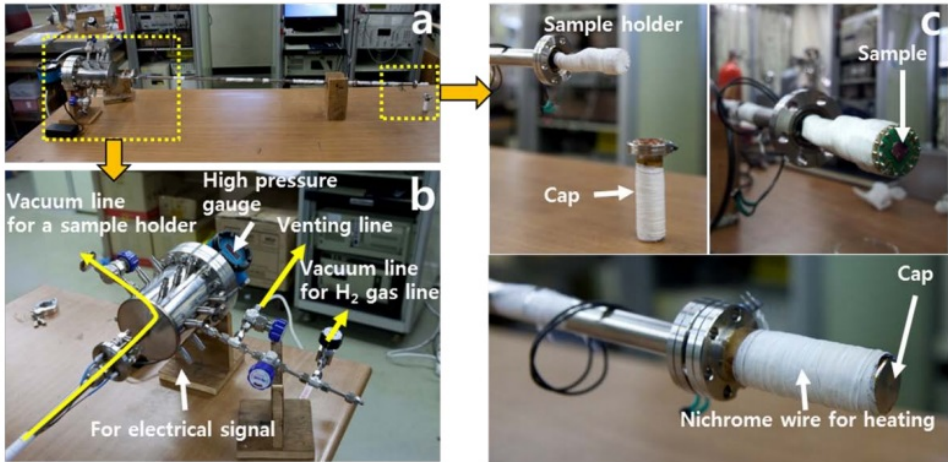


Figure 3.6: Probe for cryostat and high  $H_2$  pressure. a, Full-length photograph of the probe b, Head of the probe consisted of two vacuum lines for a sample holder and  $H_2$  gas line, venting line, high pressure gauge, and BNC type coaxial connector to sense an electrical signal. c, The sample holder is composed of a cap with nichrome wire for heating, Cu gasket, and chip holder made of Teflon [17]

and subjected to a thermal annealing procedure in high vacuum at 350 K, in order to remove some of the impurities left by the previous processing steps. The main goal of the annealing procedure was to restore the pristine conditions of the graphene and lasted for several hours until the  $V_{CNP}$  did not show any further shift. The electrical measurements done under this set of conditions represent our pristine or zero-minute exposure data. After the annealing procedure, the exposure stage started by flowing  $H_2$ , 99.9999%, pure into the chamber until the pressure reached a base value of 11 bar, preserving the temperature at 350 K. Following the exposure stage, the measurement stage was performed by keeping the base pressure steady and decreasing the temperature to 300 K. Here, the transfer curve or the Seebeck coefficient was recorded. Several exposure times on the same sample were explored by switching between exposure (300 K) and measurement stage (350 K) accordingly. The sum of the time of the subsequent exposure stages is the one that is considered in

our time-dependent studies.

Finally, when Raman spectroscopy is done on post-H<sub>2</sub> treated samples, the samples are taken out from the chamber but our graphene samples are expected to remain the hydrogenated properties due to the nature of the graphene/H<sub>2</sub> interaction, described as a chemisorption process [9].

# Bibliography

- [1] Q. Yu, J. Lian, S. Siriponglert, H. Li, Y. P. Chen, and S.-S. Pei, Applied Physics Letters **93**, 113103 (2008).
- [2] Xuesong Li, Weiwei Cai, Jinho An, Seyoung Kim, Junghyo Nah, Dongxing Yang, and Richard Piner, Science **324**, 1312–1314 (2009).
- [3] S. Bae, H. Kim, Y. Lee, X. Xu, J.-S. Park, Y. Zheng, J. Balakrishnan, T. Lei, H. Ri Kim, Y. I. Song, Y.-J. Kim, K. S. Kim, B. Özyilmaz, J.-H. Ahn, B. H. Hong, and S. Iijima, Nature Nanotechnology **5**, 574–578 (2010).
- [4] Y. Zhang, L. Zhang, and C. Zhou, Accounts of Chemical Research **46**, 2329–2339 (2013).
- [5] C.-C. Lu, Y.-C. Lin, Z. Liu, C.-H. Yeh, K. Suenaga, and P.-W. Chiu, ACS Nano **7**, 2587–2594 (2013).
- [6] Y. Wang, Y. Zheng, X. Xu, E. Dubuisson, Q. Bao, J. Lu, and K. P. Loh, ACS Nano **5**, 9927–9933 (2011).
- [7] A. W. Robertson and J. H. Warner, Nano Letters **11**, 1182–1189 (2011).
- [8] S. J. Hong, “Electrical properties of modified graphene via doping and stacking”, PhD thesis (Seoul National Univiersity, Dec. 2015).
- [9] S. J. Hong, M. Park, H. Kang, M. Lee, D. Soler-Delgado, D. S. Shin, K. H. Kim, S. Kubatkin, D. H. Jeong, Y. W. Park, et al., Applied Physics Letters **106**, 142110 (2015).

- [10] A. C. Ferrari, J. C. Meyer, V. Scardaci, C. Casiraghi, M. Lazzeri, F. Mauri, S. Piscanec, D. Jiang, K. S. Novoselov, S. Roth, and A. K. Geim, Physical Review Letters **97** (2006).
- [11] A. Das, B. Chakraborty, S. Piscanec, S. Pisana, A. K. Sood, and A. C. Ferrari, Physical Review B **79** (2009).
- [12] O. Frank, G. Tsoukleri, J. Parthenios, K. Papagelis, I. Riaz, R. Jalil, K. S. Novoselov, and C. Galotis, ACS Nano **4**, 3131–3138 (2010).
- [13] L. Malard, M. Pimenta, G. Dresselhaus, and M. Dresselhaus, Physics Reports **473**, 51–87 (2009).
- [14] A. K. Geim and K. S. Novoselov, Nature Materials, 183–191 (2007).
- [15] S.-G. Nam, D.-K. Ki, and H.-J. Lee, Physical Review B **82** (2010).
- [16] Y. M. Zuev, W. Chang, and P. Kim, Physical Review Letters **102** (2009).
- [17] B. H. Kim, S. J. Hong, S. J. Baek, H. Y. Jeong, N. Park, M. Lee, S. W. Lee, M. Park, S. W. Chu, H. S. Shin, J. Lim, J. C. Lee, Y. Jun, and Y. W. Park, Scientific Reports **2** (2012).

# Chapter 4

## N-type doping on CVD-grown twisted bilayer graphene devices by hydrogen adsorption

### 4.1 Identification of CVD-grown twisted bi-layer graphene

Among the first stages of fabrication processes of our graphene devices, the identification of the twist angle  $\theta$  of our CVD grown tBLG flakes stands out, as by classifying BLG with different stacking order, we would be able to appreciate the modifications on the carrier transport upon hydrogen exposure and put them into perspective with those previously reported on the literature. Therefore, as it has been stated before, this  $\theta$  identification procedure consisted on a cross-verification between optical microscopy and Raman spectroscopy.

By taking advantage of the high contrast of the  $\text{SiO}_2$  / graphene in-

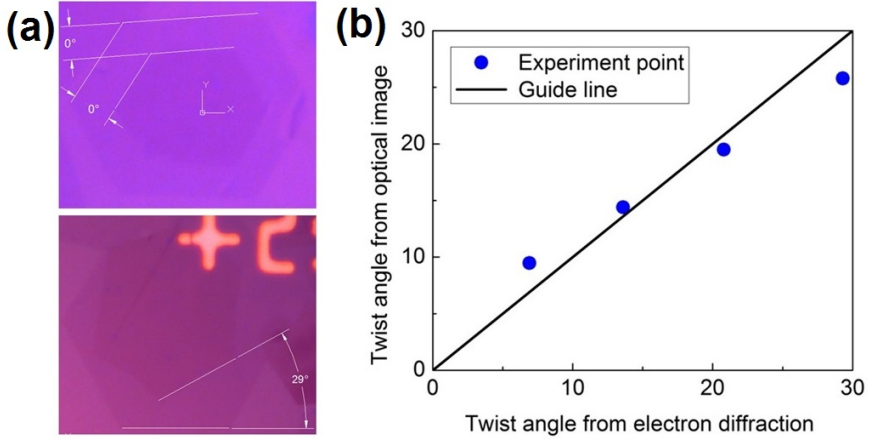


Figure 4.1: (a) Twist angle of tBLG flakes estimated by optical microscopy, (b) Correspondance of  $\theta$  between optical microscopy and TEM [1]

terface [2], we selected tBLG flakes as depicted on Figure 4.1a. The fine tuning on our growth conditions made possible to produce hexagonal shapes on the bottom and top layer of our bilayer stacks, whose edges were perfectly observed by the color change on the shadows. A previous study on these systems have related the twisting angle measured by the flake edges under optical microscopy and transmission electron microscopy, with a good agreement between the two values as shown on Figure 4.1b [1]. Therefore, on large twisted angles ( $\theta \gg 0^\circ$  but  $\theta < 30^\circ$ , due to the rotational symmetry of the system), single optical microscopy identification was used to estimate the twisted angle between the layers. However, despite the fact that optical identification gives a good estimate for large twisting angles, this method becomes uncertain for small twisting angles ( $\theta \approx 0^\circ$  and  $\theta \approx 30^\circ$ ), requiring Raman spectroscopy as a supportive method.

Figure 4.2a shows the Raman spectra of the three selected devices with small twisted angles. In agreement to what it was previously described on the last chapter, our spectra contains 4 important features:

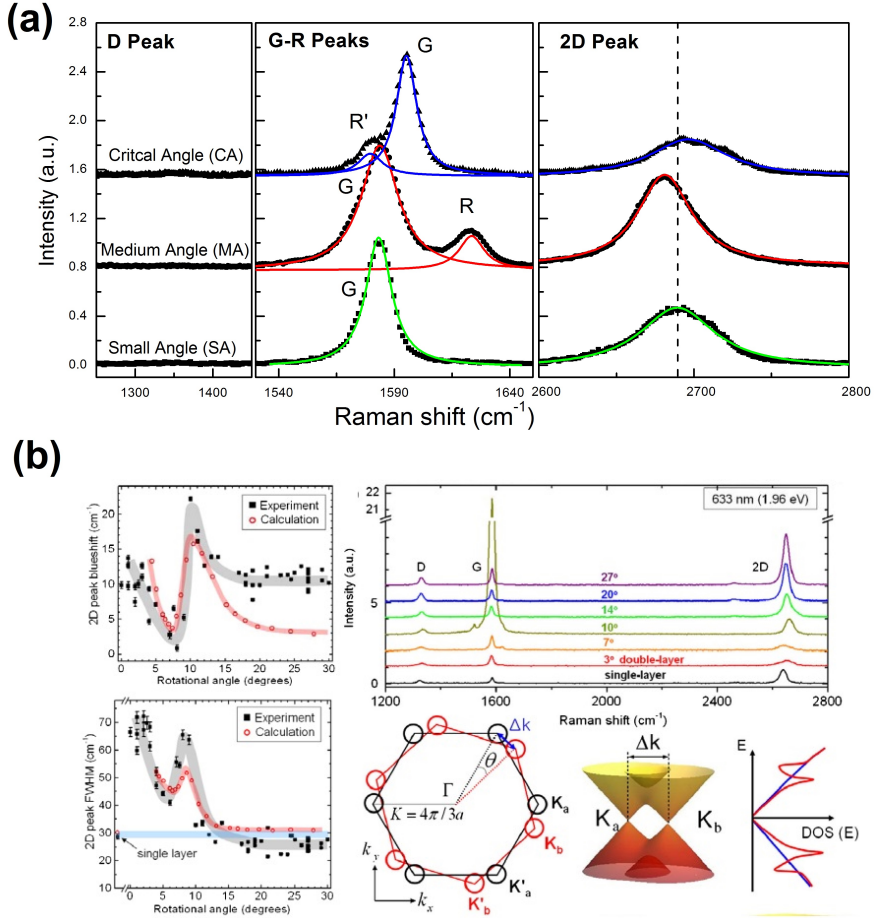


Figure 4.2: (a) Raman spectroscopy of bilayer graphene devices with different stacking angles. Colored lines represents the fitted values reported on Table 4.1. (b) Behaviour of G and 2D bands a function of  $\theta$  [3]

D, G, 2D and R-R' bands. The G and 2D peaks appears on all the graphene systems and their sensitivity to the number of layers, stacking order, doping and strain will help us to identify our samples and recognize some important features induced by the hydrogenation process. For the specific case of rotational mismatched graphenes, by tracking the evolution of the G and 2D peak, it is possible to estimate the smallest twist angles of our samples [3].

	<b>Pos (2D)</b> ( $cm^{-1}$ )	<b>FWHM (2D)</b> ( $cm^{-1}$ )	<b>I(G)/I(2D)</b> ( <i>a.u.</i> )
<b>SA</b>	2689.36	58.684	1.037
<b>MA</b>	2681.17	41.978	1.360
<b>CA</b>	2696.45	59.442	2.436

Table 4.1: Fitted values of G and 2D peaks for small angle samples. SA, MA and CA stands for small, medium and critical angle, respectively

Twisted bilayer graphene can be defined as a two non-interacting SLG with a rotational mismatch  $\theta$  between them. This angle of rotation is also reflected on the momentum space, as tBLG can be represented by two rotated SLG Brillouin zones by the same  $\theta$  angle. At sufficient small  $\theta$ , there exists some regions on the momentum space where the Dirac cones of the top and bottom layers overlap, modifying the non-interacting density of states (DOS) and giving rise to the van Hove singularities [4]. For a given  $E_L$ , it is possible to calculate the so-called critical angle value  $\theta_c$ , the twisting angle at which the laser wavelength matches the energy difference between the vHS of the valence and conduction band:

$$\theta_c = \frac{3aE_L}{\hbar v_f 4\pi} \quad \theta_c \approx 12^\circ \quad (4.1)$$

$$E_L = 2.33eV \quad (4.2)$$

where  $a$ ,  $\hbar$ ,  $v_f$ , are the monolayer graphene lattice constant, the reduced Planck constant, and the Fermi velocity ( $10^6$ ), respectively. Therefore, it is expected that for a given  $E_L$ , as  $\theta \rightarrow \theta_c$ , the Raman spectra will change dramatically as inter-layer interaction becomes stronger. As it can be seen on Figure 4.2b, the position and the FWHM have a non-monotonical behaviour as a function of  $\theta$ , with minimum between  $0^\circ$  and  $\theta_c$ . Our samples have the same trend as indicated on Table 4.1, which shows some of the fitting data for the three small angle devices, where the medium angle (MA) sample shows the lowest Pos (2D) and FWHM (2D) from the set. Moreover, the intensity ratio I(G)/I(2D) increases with the

twist angle from 1.037 of the small angle sample (SA) to 2.436 of the critical angle sample (CA), indicating that indeed, the SA, MA and the CA samples can be sorted in an increasing fashion on the twisting angle.

Finally, in addition to characteristic behaviour on the G and 2D band, the appearance of the R-R' peaks on some of the Raman spectra reinforces the correct classification given to the three selected samples. The origins of the R-R' peak bands are related with an intra-valley scattering of the electrons, which is activated by a superlattice wave-vector formed by the twisted structure and it is only visible at small twisted angles [5]. As the twisting angle develops, a satellite peak on the Raman spectrum appears to the right of the G-band at smaller angles (MA sample) and ends up vanishing on the left side of the G-peak as  $\theta$  goes near to the critical value (CA sample). For angles near zero, the Raman spectrum resembles to that of the AB-SLG and as a consequence, no R-R' peaks are noted on our measurements (SA sample). [6]

## 4.2 Transfer curves of graphene devices under hydrogen exposure

Figure 4.3 shows the transfer curves of the four devices subject to hydrogen exposure: the three devices with angles lower than  $\theta_c$  characterized by Raman spectroscopy (label as small, medium and critical for SA, MA and CA, respectively) and a fourth device with twisting angle  $\theta > \theta_c$ . For each sample, the final exposure time was around 40 hours with subsequent measurements stages in between.

There are several features on the transfer curve that are shared by all the samples regardless of the twist angle: First, the pristine condition showed a prominent shift of the  $V_{CNP}$  towards the positive

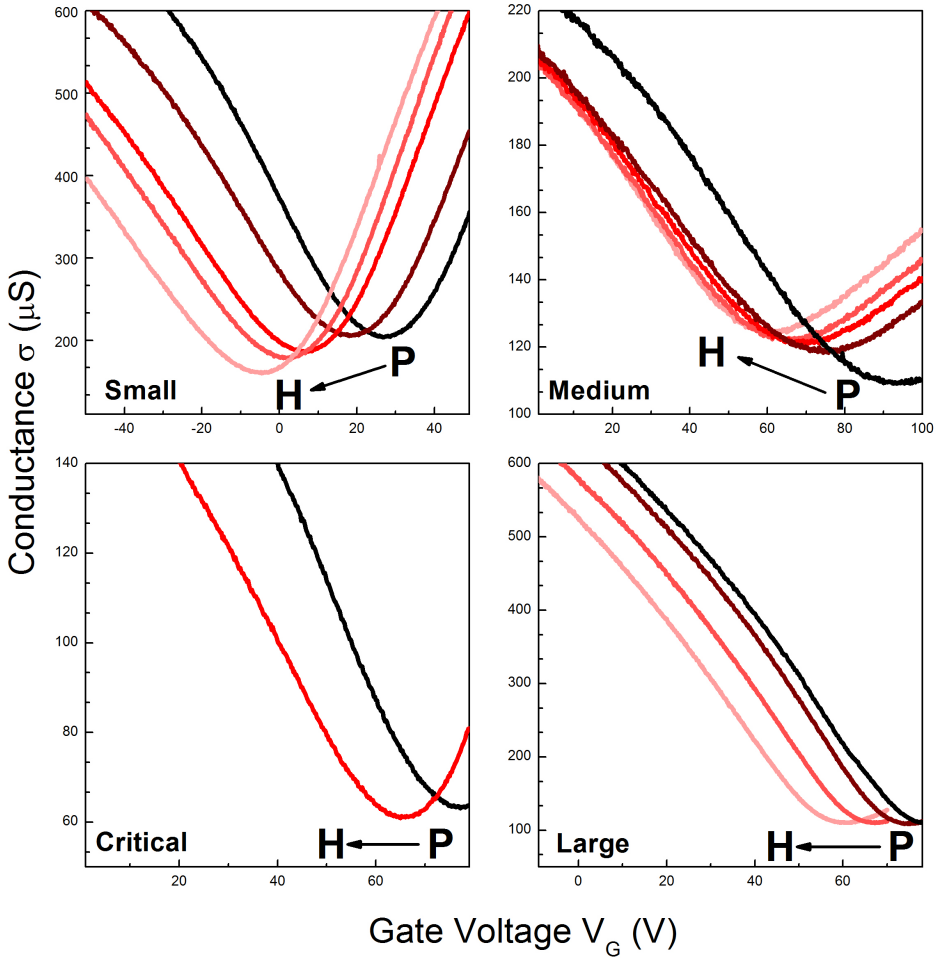


Figure 4.3: Transfer curves of all our devices as a function of time. The arrow indicates the time transient starting from the transfer curve under pristine condition (P) to the transfer curve with highest exposed sample (H). The color gradient also remarks this trend.

$V_G$  values. Whereas the reason of this hole doping behaviour cannot be uniquely determined, we would like to address two possible causes: (1) the unavoidable polymer contamination during the transfer and fabrication of the device and (2) the inclusion of external dopants due to the exposure to atmospheric conditions. Second, Upon hydrogen exposure, there is a shift on the  $V_{\text{CNP}}$  towards the negative  $V_G$  region. This

behaviour clearly demonstrate electron doping, induced by hydrogen adsorption onto the CVD-grown tBLG devices as suggested by complementary Raman spectroscopy characterization. Third, There are no insights of band gap opening. This is consistent with previously reported research on AB-stacked BLG samples [7] and finally, as exposure time develops, there occurs two phenomena in parallel: the  $V_{CNP}$  moves towards negative values exponentially and there exists an asymmetric evolution of the transfer curves. These features reveals details on the chemisorption process of hydrogen on graphene, as well as hole and electron transport through the sample.

### 4.3 Raman spectroscopy of hydrogenated tBLG

In order to support the electron doping observations on the transfer curves, Raman spectroscopy was performed on the small angle sample after hydrogen exposure (Figure 4.4a) and the fitted values are shown on Table 4.2. As a first insight, despite both G and 2D peaks show a blueshift, the 2D-peak does it in a more prominent way as  $\Delta\omega_{2D} \sim 3 cm^{-1}$  compared to the  $\Delta\omega_G = 0.38 cm^{-1}$  of the G-band.

This behaviour is better supported by using the transfer curve mea-

	Pristine	$H_2$ Exposure
$\omega_G$	$1583.26 cm^{-1}$	$1583.64 cm^{-1}$
$\Gamma_G$	$12.99 cm^{-1}$	$14.14 cm^{-1}$
$\omega_{2D(1A)}$	$2683.29 cm^{-1}$	$2686.66 cm^{-1}$
$\omega_{2D(2A)}$	$2706.80 cm^{-1}$	$2709.87 cm^{-1}$

Table 4.2: Fitted values of G and 2D peaks, before and after hydrogen exposure

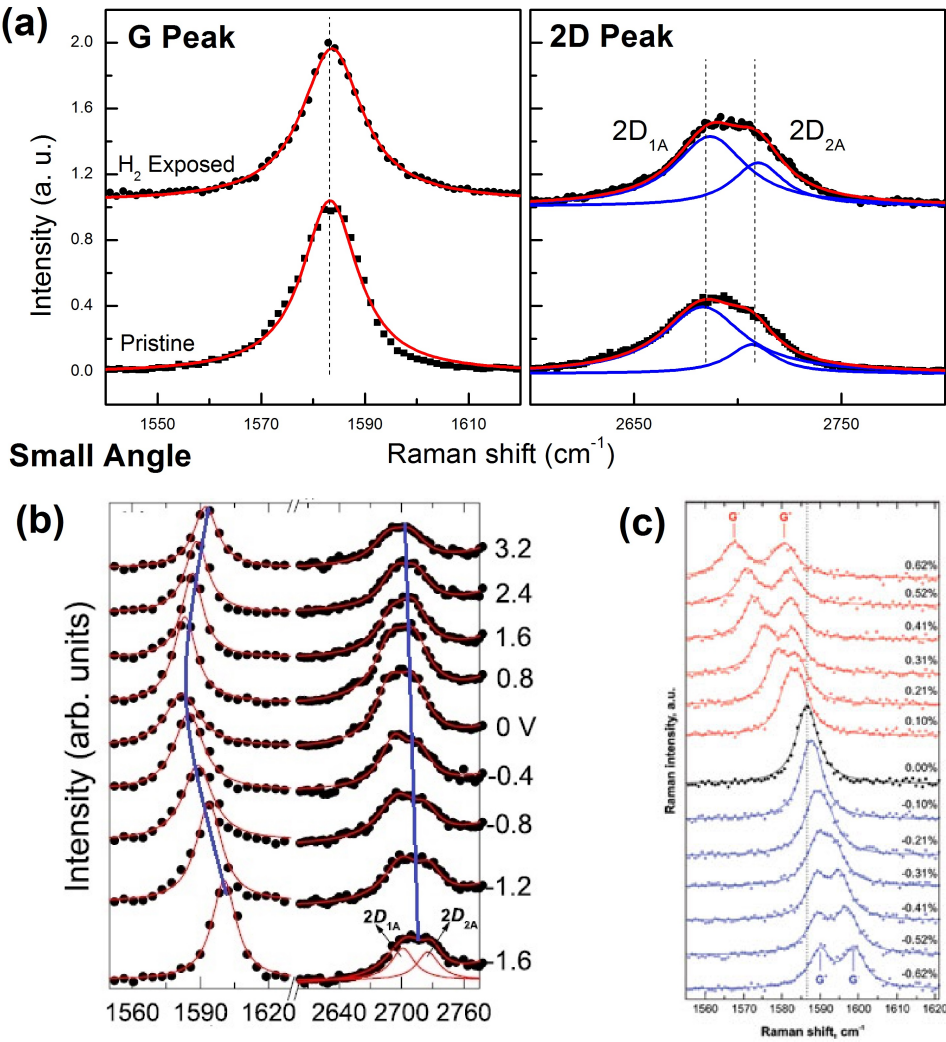


Figure 4.4: (a) Raman spectroscopy small angle sample before and after hydrogen exposure. The peak fitting information is available on Table 4.2, (b) Raman spectroscopy of BLG as a function of gating voltage, adapted from [8],(c) Raman spectroscopy of compressed graphene [9]

surments which show that our small angle device was initially hole-doped with a large positive  $V_{\text{CNP}}$  value, and it ended up on the negative  $V_G$  region, with  $V_{\text{CNP}}$  quite close to zero. In terms of the Raman spectroscopy, a pure transition of highly hole-doped to a lightly electron-doped state

would be translated into a redshift on the G-peak, with no shift on the 2D-peak as depicted on Figure 4.4b [8]. However, considering that H<sub>2</sub> dissociates on the surface of graphene, electron doping is accompanied by certain lattice compression due to the formation of the C-H bonding as it has been revealed by transmission electron microscopy [10]. Different research studies has shown that Raman spectroscopy of pure compressible strain (Figure 4.4c) blueshifts the G and the 2D peaks as a function of the strain percentage [9]. Therefore, the difference on the blueshifts between the G and 2D peak can be explained as a competition between electron doping resulting from the delocalized electron of the H<sub>2</sub> pair and lattice strain induced by the C-H formation [11]. As a result, the net effect of these both processes annihilate for the G-peak, giving as a result a smaller blueshift than the case of the 2D-peak, where the two processes enhance the shift towards the positive values of the Raman spectrum.

## 4.4 TEP measurements of graphene device under hydrogen exposure

In addition to the post-hydrogenation Raman spectroscopy measurements, the Seebeck coefficient of the critical degree angle was measured as depicted on Figure 4.5. It is important to notice that the measurements were stopped at 80 V in order to keep the integrity of the samples. Although the swept V<sub>G</sub> region was not large enough to cover that of electron transport, our measurements are still sufficient to recognize the features that supports our observations of electron doping.

At first insight, the Seebeck coefficient curve has all the features as previously described for graphene systems before and after hydrogenation [12]. However, there is a shift on the point where S = 0 towards a negative V<sub>G</sub> value after hydrogen exposure. As it has been discussed be-

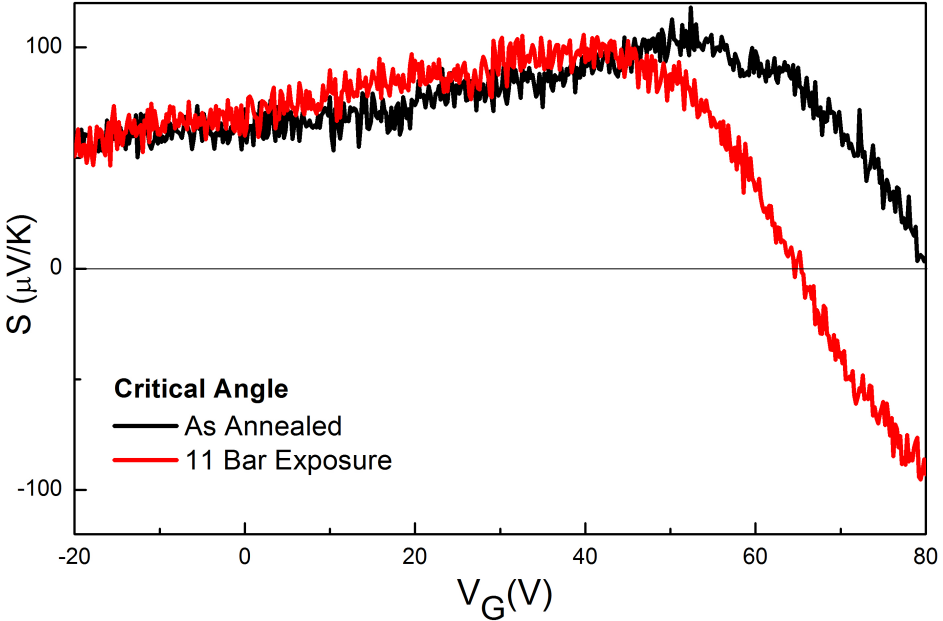


Figure 4.5: Seebeck coefficient for the critical angle sample before and after hydrogen exposure

fore, this transition point on the Seebeck coefficient indicates the change from holes to electrons as the main carriers of the sample and agrees with the shift on the  $V_{CNP}$  from 65.81 V to 77.40 V seen on the transfer curves measurements.

Furthermore, the maximum Seebeck coefficient value on the hole regime rounds on the  $120 \mu V/K$  which is consistent with those previously values measured on BLG samples and it is not enhanced nor decreased after hydrogenation. As for the characteristics far from the Dirac point, the tendency of  $S \rightarrow 0$  as  $V_G \rightarrow -\infty$  in pristine and hydrogenated cases is preserved. Since  $S$  can be interpreted as the entropy per carrier, this indicates the existence of a degenerate state in the highly doped limit, consistent in both measurements [13]. Therefore, because of the conservation on the shape and characteristics on the Seebeck coefficient

measurements upon H<sub>2</sub> treatments, we can conclude that upon exposure to the molecular hydrogen environment, the n-type doping process in twisted BLG graphene does not change prominently its electronic structure, in agreement with similar studies done on SLG [11].

## 4.5 Development of device features as hydrogen exposure

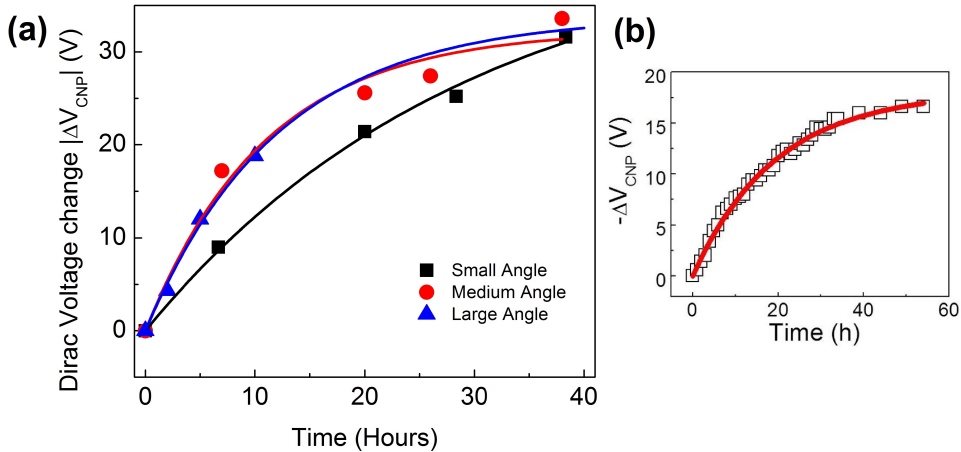


Figure 4.6: (a)  $V_{CNP}$  for different twisted angles as a function of time. The fitted exponential functions on the  $V_{CNP}$  plot correspond to the first-order absorption process (b) First-order adsorption process of H<sub>2</sub> on a BLG / h-BN device [7]

Lastly, in spite of obtaining further information to describe our transfer curves (Figure 3.4), the  $V_{CNP}$  and the carrier mobilities are studied as a function of time exposure. Figure 4.6a shows the  $V_{CNP}$  difference with respect of the pristine condition, as a function of time. ( $|\Delta V_{CNP}|(t) = |V_{CNP}^{Pristine} - V_{CNP}(t)|$ ) It is clearly seen that, for all the twisting angles,  $\Delta V_{CNP}$  can be perfectly fitted by an exponential func-

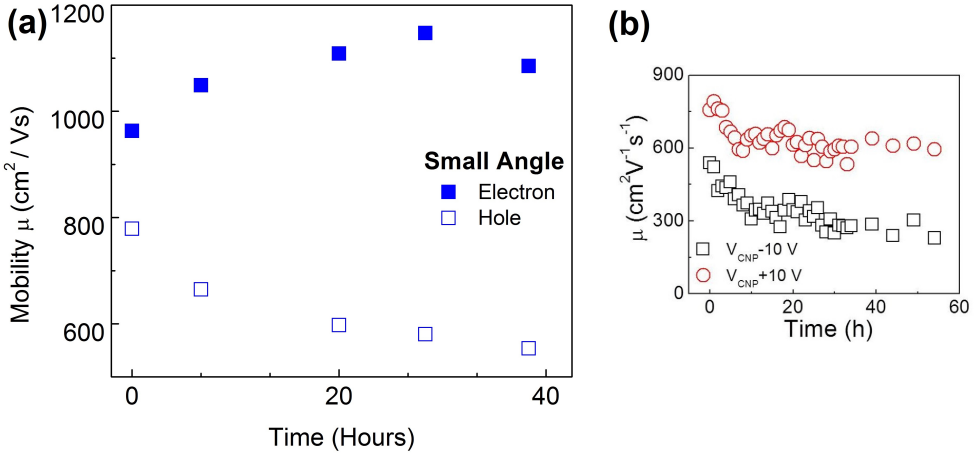


Figure 4.7: Evolution of carrier mobility as a H<sub>2</sub> time exposure for (a) Our sample tBLG / SiO<sub>2</sub> (b) BLG / h-BN device [7]

tion:

$$\Delta V_{CNP} = \Delta V_{CNP0}(1 - e^{-kt}) \quad (4.3)$$

Due to the fact that the  $\Delta V_{CNP}$  can be related with the impurity carrier density by  $n_{imp} = (C_G/e)|\Delta V_{CNP}|$ , the exponential behaviour on the  $V_{CNP}$  as a function of time represents a first order adsorption model of the hydrogen molecules onto the graphene surface [14]. Moreover, this adsorption model has been observed on exfoliated BLG / h-BN structure (Figure 4.6b), where substrate intercalation of hydrogen can be mitigated [7], indicating that the hydrogen dissociation at high temperature follows the same path and it is intrinsic of bilayer graphene samples, regardless of the extra internal degree of complexity  $\theta$

The other interesting feature on the transfer curve is the asymmetric evolution of the electrons and hole mobilities as a function of time exposure (Figure 4.7a). The mobilities were extracted from the transfer curves by using the following relation:

$$\mu_c = \frac{1}{C_G} \frac{d\sigma}{dV_G} \quad (4.4)$$

where  $\mu$  is the mobility of holes ( $c = h$ ) or electrons ( $c = e$ ),  $C_G = 115 \text{ aF}/\mu^2$  is the capacitance per unit area and  $\sigma$  is the conductance of the sample. The derivative term was taken from the slope of the linear region at the left or right of the charge neutrality point for holes or electrons, respectively [15]. Figure 4.7a contains the graph described above, showing that the electron mobility increases as a function of time, while the hole mobility does the opposite. This asymmetric evolution of the mobilities is better understood if we consider the same BLG / h-BN studies as before. Due to the fact that the  $\text{SiO}_2$  impurities are suppressed by the h-BN substrate, the BLG on the top does not suffer of any other scattering mechanism rather than the hydrogen impurities and those coming from the graphene itself. Consequently, there exists a pure decrease on the electron and hole mobilities (Figure 4.7b) due to the fact that the dissociated hydrogen has been catalogued as a short-range scatterer [16].

However, when graphene is placed over bare  $\text{SiO}_2$ , its roughness, impurities and dangling bonds can act as a scatterers centers increasing the electron mobility and hindering the pure effects that the hydrogen adsorption has on graphene. The mobility asymmetry caused by the substrate has been observed on exfoliated BLG upon hydrogen [10] and oxygen [14] exposure. Therefore, while hydrogen adsorption on CVD-grown tBLG might act as a short-range scatterer as well, there is a need of reproduce further experiments by using high-quality substrates, to reduce the external perturbations, and different stacking angles  $\theta$ , to explore the interlayer interactions and generalize the results for the BLG systems.

# Bibliography

- [1] S. J. Hong, “Electrical properties of modified graphene via doping and stacking”, PhD thesis (Seoul National Univiversity, Dec. 2015).
- [2] P. Blake, E. W. Hill, A. H. Castro Neto, K. S. Novoselov, D. Jiang, R. Yang, T. J. Booth, and A. K. Geim, *Applied Physics Letters* **91**, 063124 (2007).
- [3] K. Kim, S. Coh, L. Z. Tan, W. Regan, J. M. Yuk, E. Chatterjee, M. F. Crommie, M. L. Cohen, S. G. Louie, and A. Zettl, *Physical Review Letters* **108** (2012).
- [4] R. W. Havener, H. Zhuang, L. Brown, R. G. Hennig, and J. Park, *Nano Letters* **12**, 3162–3167 (2012).
- [5] V. Carozo, C. M. Almeida, E. H. M. Ferreira, L. G. Cançado, C. A. Achete, and A. Jorio, *Nano Letters* **11**, 4527–4534 (2011).
- [6] C.-H. Yeh, Y.-C. Lin, Y.-C. Chen, C.-C. Lu, Z. Liu, K. Suenaga, and P.-W. Chiu, *ACS Nano* **8**, 6962–6969 (2014).
- [7] S. J. Hong, H. Kang, M. Park, M. Lee, D. Soler-Delgado, D. H. Jeong, Y. W. Park, and B. H. Kim, *RSC Adv.* **5**, 103276–103279 (2015).
- [8] A. Das, B. Chakraborty, S. Piscanec, S. Pisana, A. K. Sood, and A. C. Ferrari, *Physical Review B* **79** (2009).
- [9] O. Frank, G. Tsoukleri, J. Parthenios, K. Papagelis, I. Riaz, R. Jalil, K. S. Novoselov, and C. Galiotis, *ACS Nano* **4**, 3131–3138 (2010).

- [10] B. H. Kim, S. J. Hong, S. J. Baek, H. Y. Jeong, N. Park, M. Lee, S. W. Lee, M. Park, S. W. Chu, H. S. Shin, J. Lim, J. C. Lee, Y. Jun, and Y. W. Park, *Scientific Reports* **2** (2012).
- [11] S. J. Hong, M. Park, H. Kang, M. Lee, D. Soler-Delgado, D. S. Shin, K. H. Kim, S. Kubatkin, D. H. Jeong, Y. W. Park, et al., *Applied Physics Letters* **106**, 142110 (2015).
- [12] Y. M. Zuev, W. Chang, and P. Kim, *Physical Review Letters* **102** (2009).
- [13] S.-G. Nam, D.-K. Ki, and H.-J. Lee, *Physical Review B* **82** (2010).
- [14] I. Silvestre, E. A. de Morais, A. O. Melo, L. C. Campos, A.-M. B. Goncalves, A. R. Cadore, A. S. Ferlauto, H. Chacham, M. S. C. Mazzoni, and R. G. Lacerda, *ACS Nano* **7**, 6597–6604 (2013).
- [15] K. S. Novoselov, A. K. Geim, S. V. Morozov, D. Jiang, M. I. Katsnelson, I. V. Grigorieva, S. V. Dubonos, and A. A. Firsov, *Nature* **438**, 197–200 (2005).
- [16] J. Katoch, J.-H. Chen, R. Tsuchikawa, C. W. Smith, E. R. Mucciolo, and M. Ishigami, *Physical Review B* **82** (2010).

# Chapter 5

## Summary and Conclusion

In summary, hexagonal twisted bilayer graphene was synthesized by Atmospheric Pressure Chemical Vapor Deposition and transferred to  $\text{SiO}_2$  substrates. Optical microscopy and Raman spectroscopy were used to estimate the twist angle  $\theta$  on the tBLG flakes. After the angle identification, the tBLG flakes were etched and four devices with different stacking angles, ranging from small to large twist, were fabricated. The devices were build either on field-effect transistor or thermoelectric power configuration. Finally, the four devices were subjected to 11 bar of pure hydrogen at 350 K inside of a high-pressure/high-vacuum chamber, where all the measurements were performed.

As a result of hydrogenation, it was found that all the devices, regardless of  $\theta$ , showed a N-type doping behaviour upon hydrogen exposure. This effect was notorious on the transfer curves as the  $V_{\text{CNP}}$  shifts towards negative values as the exposure time increases. By measuring the Seebeck coefficient ( $S$ ) as a function of  $V_G$  on the small angle sample, the negative shift on the zero-crossing point of  $S$  supported the observation of electron doping as seen on the transfer curves, and the unaffected shape of the  $S$  curve indicates the preservation of the electronic structure similar to the SLG case. Furthermore, post-hydrogenation Raman spec-

troscopy studies showed a unbalanced blue-shift on the G and 2D peaks, resulted from the competition between electron doping and lattice compression, suggesting the formation of the C-H bond due to dissociation of the H<sub>2</sub> molecule on the CVD-grown tBLG surface, in agreement with previous studies.

Finally, in spite of exploring the evolution of the hydrogenation process, the change of the V<sub>CNP</sub> and the carrier mobilities were extracted from the transfer curves and studied as a function of time. For the case of the V<sub>CNP</sub>, since  $|\Delta V_{CNP}| \propto n_{imp}$ , the exponential trend of our curves follows a first-order adsorption model of the hydrogen atoms on graphene, by which it is possible to estimate of the rate of the C-H bond formation and the available carbon sites due to the limited nature of the process. Moreover, this behaviour has been previously observed in exfoliated BLG samples and appears to be an intrinsic feature of bilayer graphene systems. Similarly, the evolution of the carrier mobilities of the tBLG flakes showed an exponentially asymmetric behaviour for electrons and holes, increasing for former and decreasing for latter. This characteristic evolution is better understood by taking account the substrate effects, which hinders the decreasing effect in both mobilities of hydrogen adsorbates as they been classified as short-range scatterers

Therefore, while the present work helps in understanding the hydrogenation process on bilayer graphene with different stacking configurations, there is a need to extend the hydrogenation studies of CVD-grown tBLG over high-quality substrates to have a clearer picture on the evolution of the hydrogen interaction with tBLG and understand the its role on the carrier transport in graphene.

## 국문 초록

그래핀의 수소흡착은 전자 도핑과 같은 수송 특성의 변화로 인해 주목을 끈다. 박리형 그래핀의 수소결합에 대한 연구는 현재까지 이루어졌으나 틀어진 이중층 그래핀과 같이 더 높은 자유도가 주어진 이중층 그래핀 시스템의 경우에 대한 특성 연구는 많이 이루어지지 않고 있다. 이 논문에서 우리는 화학기상증착법(CVD)으로 키운, 이중층 그래핀 소자를 고기압의 수소 환경에 노출시켰다. 라만 분광법을 비롯해 전기 전도도 및 제벡 계수 측정법과 같은 전기적 특성 변화를 통해, 층 간 각도에 무관하게 그래핀 표면에서 수소 해리에 의한 흡착 현상에 기인한 n-타입 도핑 현상이 확인되었다. 이 연구 결과를 통해 수소와 결합된 이중층 그래핀 소자의 기능 변화 및 응용성 연구에 도움을 받을 수 있을 것이다.

키워드 : 틀어진 이중층 그래핀, 수소결합, 전자 도핑, 제벡 계수